ATL-PHYS-PROC-2021-005
22 February 2021

Search for heavy resonances decaying into a pair of Z bosons using 139 fb^{-1} of p–p collisions at $\sqrt{s}$ = 13 TeV with the ATLAS detector

Theodota Lagouri[1]
On behalf of the ATLAS Collaboration

[1] Instituto de Alta Investigación, Universidad de Tarapacá, Arica, Chile

E-mail: theodota.lagouri@cern.ch

This paper presents the search for heavy resonances decaying into a pair of Z bosons leading to the $\ell^+\ell^-\ell'^+\ell'^-$ and $\ell^+\ell^-\nu\bar{\nu}$ final states, where ℓ stands for either an electron or a muon. The search uses proton-proton collision data at a centre-of mass energy of 13 TeV collected with the ATLAS detector from 2015 to 2018 corresponding to an integrated luminosity of 139 fb^{-1}, which is the full data statistics collected during the Run 2 of the Large Hadron Collider (LHC). The mass range for the hypothetical resonances considered spans from 200 GeV to 2000 GeV. In the absence of an observed significant excess, the results are interpreted as upper limits on the production cross section of a spin-0 or spin-2 resonance. The upper limits for the spin-0 resonance are interpreted to exclusion contours in the context of Type-I and Type-II two-Higgs-doublet models (2HDM), while those for the spin-2 resonance are used to constrain the Randall-Sundrum (RS) model with an extra dimension giving rise to spin-2 graviton excitations.

Contents

1 Introduction

In 2012, the ATLAS and CMS collaborations at the LHC discovered a new particle [1, 2], an important milestone in the understanding of the mechanism of electroweak (EW) symmetry breaking. Subsequent studies [3–5] have shown that the properties of the new particle are consistent with those of the Standard Model (SM) Higgs boson. Several extensions to the SM imply that this new particle could be part of an extended scalar sector and predict additional Higgs bosons motivating searches in an extended mass range. Many of these models predict the existence of new heavy resonances decaying into dibosons. In models with an extended Higgs sector, such as the two-Higgs-doublet models (2HDM) [6], a heavy spin-0 neutral Higgs boson (H) can decay into a pair of Z bosons. In models with warped extra dimensions [7, 8] spin-2 Kaluza-Klein (KK) excitations of the graviton (GKK) are expected to decay into ZZ.

This paper reports on two searches for heavy resonances decaying into two SM Z bosons, leading to the $\ell^+\ell^-\ell'^+\ell'^-$ and $\ell^+\ell^-\nu\bar{\nu}$ final states, where ℓ stands for either an electron or a muon and ν stands for any of the three neutrino flavours [9]. The data used were recorded by the ATLAS detector between 2015 and 2018 in proton-proton collisions at $\sqrt{s}$ = 13TeV (Run 2) at the Large Hadron Collider (LHC) and correspond to an integrated luminosity of 139 fb^{-1}.

The additional Higgs boson (spin-0 resonance), denoted by H throughout this paper, is assumed to be produced mainly via gluon-gluon fusion (ggF) and vector-boson fusion (VBF) processes with the ratio of the two production mechanisms unknown in the absence of a specific model. The results are interpreted separately for the ggF and VBF production modes, with events being classified into ggF- and VBF-enriched categories in both final states. The searches cover a wide mass range from 200 GeV up to 2000 GeV and look for an excess in the distribution of the the four-lepton invariant mass, $m_{4\ell}$, for the $\ell^+\ell^-\ell'^+\ell'^-$ final state, and the transverse mass, m_T, for the $\ell^+\ell^-\nu\bar{\nu}$ final state, as the escaping neutrinos do not allow the full reconstruction of the final state.

In the absence of such an excess, limits on the production rate of different signal hypotheses are obtained from a simultaneous likelihood fit in the two final states. By combining the $\ell^+\ell^-\ell'^+\ell'^-$ and the $\ell^+\ell^-\nu\bar{\nu}$ final states the overall sensitivity is improved due to the good mass resolution of the first and the large branching ratio of the second final state.

First, the hypothesis of a heavy Higgs boson in the narrow-width approximation (NWA) is studied. The upper limits on the production rate of a heavy Higgs boson are also translated into exclusion contours in the context of the two-Higgs-doublet model (2HDM). Then, large-width assumption (LWA) models [6], assuming widths of 1%, 5%, 10% and 15% of the resonance mass, are examined only for ggF production, which dominates over the next-largest contribution (VBF) in the search range, as several theoretical models favour non-negligible natural widths. Results are also interpreted assuming the bulk Randall-Sundrum (RS) model with a warped extra dimension giving rise to a spin-2 Kaluza-Klein (KK) excitation of the graviton G_{KK}.

In the previous publication [10], which combined the search of the two final states ($\ell^+\ell^-\ell'^+\ell'^-$ and $\ell^+\ell^-\nu\bar{\nu}$) using the Run 2 early dataset 2015-2016 of 36 fb^{-1}, hints for two excesses were observed in the data in the $\ell^+\ell^-\ell'^+\ell'^-$ search for $m_{4\ell}$ around 240 and 700 GeV, each with a local significance of 3.6σ estimated in the asymptotic approximation, assuming the signal comes only from ggF production. The excess at 240 GeV was observed mostly in the 4e channel, while the one at 700 GeV was observed in all channels and categories. No significant deviation from the expected background was observed in the $\ell^+\ell^-\nu\bar{\nu}$ final state. The excess observed in the $\ell^+\ell^-\ell'^+\ell'^-$ search at a mass around 700 GeV is excluded at 95% confidence level (CL) by the $\ell^+\ell^-\nu\bar{\nu}$ search, which was more sensitive in this mass range. The excess at 240 GeV was not covered by the $\ell^+\ell^-\nu\bar{\nu}$ search, as the sensitivity of this channel started at 300 GeV.

The main improvements reported in this study [9] relative to the previous published search [10] are the following: i) the full LHC Run 2 integrated luminosity is used; ii) both analyses ($\ell^+\ell^-\ell'^+\ell'^-$ and $\ell^+\ell^-\nu\bar{\nu}$) profit from improved lepton reconstruction and isolation selection, reducing the impact of additional p-p interactions in the same or neighbouring bunch crossing (pile-up); iii) also, they both profit from improved jets reconstruction using a particle-flow algorithm which combines measurements from the tracker and the calorimeter; iv) for both analyses, the normalisation of the SM ZZ background is derived from data rather than being estimated from SM predictions; v) incorporate the VBF category and large-width approximation

(LWA) signal parameterisation into both analyses; vi) the event classification targeting different production processes is optimised using machine learning (ML) algorithms in the case of $ZZ \to \ell^+\ell^-\ell'^+\ell'^-$ final state; vii) the m_T distribution is used to search for signals in the VBF-enriched category in the case of the $ZZ\to\ell^+\ell^-\nu\bar{\nu}$ final state, (in addition to the use of m_T in the ggF-enriched category); and viii) the signal search mass range is extended up to 2000 GeV. The aim of the improved analyses [9] is to reduce the expected upper limit on the production cross section of an additional heavy resonance in comparison with the previous published result [10] scaled to the full Run 2 luminosity.

2 ATLAS detector

The ATLAS experiment is a multipurpose detector with a forward–backward symmetric cylindrical geometry and a solid-angle coverage of nearly 4π; a detailed description can be found in [11].

The inner detector is surrounded by a thin superconducting solenoid providing a 2T magnetic field, and by a finely segmented lead/liquid-argon (LAr) electromagnetic calorimeter covering the region $|\eta| < 2.3$. A steel/scintillator-tile hadron calorimeter provides coverage in the central region $|\eta| < 1.7$. The endcap and forward regions, covering the pseudorapidity range $1.5 < |\eta| < 4.9$, are instrumented with LAr electromagnetic and hadronic calorimeters, with steel, copper, or tungsten as the absorber material. A muon spectrometer (MS) system incorporating large superconducting toroidal air-core magnets surrounds the calorimeters. Three layers of precision wire chambers provide muon tracking in the range $|\eta| < 2.7$, while dedicated fast chambers are used for triggering in the region $|\eta| < 2.4$. The trigger system, composed of two stages, was upgraded [12] before Run 2. The first stage uses information from the calorimeters and muon chambers to select events from the 40 MHz bunch crossings at a maximum rate of 100 kHz. The second stage, called the high-level trigger (HLT), reduces the data acquisition rate to about 1 kHz on average. The HLT is software-based and runs reconstruction algorithms similar to those used in the offline reconstruction.

3 Data and simulation

3.1 Data

The proton-proton (p-p) collision data used in these searches were collected by the ATLAS detector at a centre-of-mass energy of 13 TeV with a 25 ns bunch-spacing configuration from 2015 to 2018 (Run 2). The data are subjected to quality requirements: if any relevant detector component was not operating correctly during the period in which an event was recorded, the event is rejected. The efficiency for recording good-quality data during Run 2 is 95.6% [13].

3.2 Simulation

Monte Carlo (MC) simulated events are used for signal and background modelling, the determination of some of the background contributions, the evaluation of the signal acceptance, optimisation of event selection, estimation of systematic uncertainties and the statistical analysis [9].

The events produced by each Monte Carlo (MC) event generator were processed through the ATLAS detector simulation [14] using the Geant4 framework [15]. Additional inelastic p-p interactions (pile-up) were overlaid on the simulated signal and background events [16–18]. The simulated events are weighted to reproduce the observed distribution of the mean number of interactions per bunch crossing in data (pile-up reweighting)

3.2.1 Signal simulation

Many models beyond the Standard Model of particle physics predict heavy particles that could decay into diboson final states. Below a subset of the models predicting a heavy ZZ resonance is described.

3.2.1.1 Heavy Higgs-like Scalar

One model considered here is that of a heavy Higgs decay, including both the Narrow Width Approximation (NWA) and the Large Width Approximation (LWA). Large width samples are produced only for ggF production.

Heavy spin-0 resonance production was simulated using the Powheg-Box [19] MC event generator [20–23]. The gluon-gluon fusion and vector-boson fusion production modes were simulated separately, with matrix elements calculated to next-to-leading-order (NLO) accuracy in quantum chromodynamics (QCD).

Events from ggF and VBF production were generated in the resonance mass range of 300 GeV to 2000 GeV in the NWA, using a step size of 100 GeV up to 1000 GeV and 200 GeV above. For the $\ell^+\ell^-\ell'^+\ell'^-$ final state, due to the sensitivity of the analysis at lower masses, events were also generated for $m_H = 200$ GeV. In addition, events from ggF heavy Higgs production with a width of 15% of the Higgs boson mass m_H were generated at NLO accuracy in QCD using MadGraph5_aMC@NLO [24, 25] Events were generated in the resonance mass range of 400 GeV to 2000 GeV using a step size of 100 (200) GeV up to (above) 1000 GeV. Similarly, events with a width of 5% or 10% of $m_H = 900$ GeV were generated for validating the analytic parameterization of the $m_{4\ell}$ distribution used in the $\ell^+\ell^-\ell'^+\ell'^-$ final state as described in Section 5.4. For the $\ell^+\ell^-\nu\bar{\nu}$ final state, a reweighting procedure is used on fully simulated events to obtain the reconstructed m_T distribution at any value of mass and width tested.

3.2.1.2 Graviton

The Randall-Sundrum (RS1) framework attempts to explain the hierarchy problem by introducing large extra dimensions in which SM fields can propagate. This leads to a tower of Kaluza-Klein (KK) excitations of SM fields, notably including KK excitations of the gravitational field that appear as TeV-scale spin-2 Gravitons (G_{KK}) [8, 26].

In some RS1 models the graviton has sizeable couplings to all SM fields, which do not propagate significantly into the extra dimension (bulk). This leads to large production rates in both gluon-gluon (gg) and quark-quark (qq) fusion modes, and substantial decay rates to diphotons and dileptons. In the "bulk RS" scenario considered here, however, the SM fields are permitted to propagate into the bulk, where they are localised. The bulk RS model avoids the constraints on other RS scenarios arising from flavour physics and electroweak precision tests, at the cost of suppressing the couplings of the G_{KK} to light fermions, which leads to significantly reduced production rates from qq fusion and lower branching fractions to leptons and photons. The gg fusion production mode therefore dominates in the bulk RS model, with the G_{KK}-gluon coupling suppressed by a factor $k/\bar{M}_{Pl}$, where k is the curvature scale of the extra dimension and $\bar{M}_{Pl} = M_{Pl}/\sqrt{8\pi}$ is the reduced Planck mass. The value of $k/\bar{M}_{Pl}$ is typically of order 1, and along with the mass of the G_{KK} is the only free parameter in this simplified model. The decays of the GKK in this scenario are dominated by $G_{KK} \to t\bar{t}$, $G_{KK} \to HH$, and $G_{KK} \to V_L V_L$, with branching fractions that depend on mass.

Spin-2 Kaluza-Klein gravitons from the bulk Randall-Sundrum model were generated with MadGraph5_aMC@NLO at LO accuracy in QCD [27]. Here, the dimensionless coupling $k/\bar{M}_{Pl}$ is set to 1. The width of the resonance is correlated with the coupling $k/\bar{M}_{Pl}$ and in this configuration it is around $\approx 6\%$ of its mass. Mass points between 600 GeV and 2 TeV with 200 GeV spacing were generated for both final states.

3.2.2 Background

Background processes include diboson (ZZ, WW, WZ), triboson (WWZ, ZZZ, WZZ), Z+jets, $t\bar{t}$ and $t\bar{t}V$ (V=W or Z) productions.

The $q\bar{q} \to ZZ$ background was simulated by the Sherpa generator [27–34], NLO electroweak (EW) corrections were applied as a function of $m_{4\ell}$ for the $\ell^+\ell^-\ell'^+\ell'^-$ final state [35, 36], and as a function of the transverse momentum of the Z boson that decays into two neutrinos for the $\ell^+\ell^-\nu\bar{\nu}$ final state [30, 37–40].

The EW production of a ZZ pair and two additional jets via vector-boson scattering was generated using Sherpa for both the $\ell^+\ell^-\ell'^+\ell'^-$ and $\ell^+\ell^-\nu\bar{\nu}$ final states, where the process $ZZZ \to 4\ell qq$ was also taken into account.

In addition, the WZ diboson events from both QCD and EW production, with the subsequent leptonic decays of both the W and Z bosons, were simulated by Sherpa with a similar set-up. Finally, WZ events with the Z boson decaying leptonically and the W boson decaying hadronically were modelled with Sherpa.

The $gg \to ZZ$ process was modelled by Sherpa at LO accuracy in QCD for both final states, including the off-shell SM h boson contribution and the interference between the h and ZZ processes. The higher-order correction factor accounting for up to NLO accuracy in QCD for the $gg \to ZZ$ continuum production was calculated [41–44], including the $gg \to h^* \to ZZ$ process [45]. Based on these studies, a constant factor of 1.7 is used, and a relative uncertainty of 60% is assigned for the normalisation in both searches.

For the $\ell^+\ell^-\nu\bar{\nu}$ final state, the contribution from WW production was removed in the Sherpa simulation of the $q\bar{q} \to WW$ and $gg \to WW$ processes by requiring the charged leptons and the neutrinos to have different lepton flavours. The $q\bar{q} \to WW$ and $gg \to WW$ processes were then modelled with Powheg-Box and Sherpa, respectively. The interference between WW and ZZ production is expected to be negligible [38] and is therefore not considered.

Events containing a single Z boson with associated jets were simulated using the Sherpa event generator. The Z+jets events are normalised using the NNLO cross sections [46]. The triboson backgrounds ZZZ, WZZ, and WWZ with fully leptonic decays and at least four prompt charged leptons were modelled using Sherpa with LO accuracy of the QCD calculations. The simulation of $t\bar{t} + V$ production ($V = W$ or Z) with both top quarks decaying semi-leptonically and the vector boson decaying inclusively was done with MadGraph5_aMC@NLO. The total cross section is normalised to the prediction [47], which includes the two dominant terms at both LO and NLO. The $t\bar{t}$ background, as well as single-top and Wt production, were modelled using Powheg-Box.

In order to study the interference treatment for the LWA case, samples containing the $gg \to ZZ$ continuum background (B) as well as its interference (I) with a hypothetical heavy Higgs signal (S) were used and are referred to as SBI samples hereafter. In the $\ell^+\ell^-\ell'^+\ell'^-$ final state the MCFMNLO event generator [48] was used to produce SBI samples where the width of the heavy scalar was set to 15% of its mass, for masses of 200, 300, 400, 500, 600, 800, 1000, 1200, and 1400 GeV. Background-only samples were also generated with the MCFM event generator; these are used to extract the signal-plus-interference term (SI) by subtracting them from the aforementioned SBI samples. For the $\ell^+\ell^-\nu\bar{\nu}$ final state, the SBI samples were generated with the $gg2VV$ event generator [49, 50]. The samples include signal events with a scalar mass of 400, 700, 900, 1200, and 1500 GeV.

4 Object and Event Reconstruction

Selected electrons [51, 52] have $p_T > 4.5$ GeV and $|\eta| < 2.47$. The $\ell^+\ell^-\ell'^+\ell'^-$ analysis uses a 'loose' WP, with an efficiency of at least 90% for electrons with $p_T > 30$ GeV [53]. The 'medium' WP (with an efficiency about 85% for electrons with $p_T > 30$ GeV) is adopted to select candidate electrons in the $\ell^+\ell^-\nu\bar{\nu}$ analysis.

The minimum p_T for muon candidates is 5 GeV, while the maximum $|\eta|$ is 2.7. A "loose" muon identification WP, which uses all muon types, is adopted by the $\ell^+\ell^-\ell'^+\ell'^-$ analysis. This criterion has an efficiency of at least 98% [54] for isolated muons with $p_T = 5$ GeV and rises to 99.5% at higher p_T. For the $\ell^+\ell^-\nu\bar{\nu}$ analysis a "medium" WP is used, which only includes combined muons and has an efficiency of 98%.

Jets [55–58] to be used are required to satisfy $p_T > 30$ GeV and $|\eta| < 4.5$. Jets from pile-up with $|\eta| < 2.5$ are suppressed using a jet-vertex-tagger multivariate discriminant [59, 60]. Jets containing b-hadrons, referred to as b-jets, are identified by the long lifetime, high mass, and decay multiplicity of b-hadrons, as well as the hard b-quark fragmentation function. The $\ell^+\ell^-\nu\bar{\nu}$ analysis identifies b-jets of $p_T > 20$ GeV and $|\eta| < 2.5$ using an algorithm that achieves an identification efficiency of about 85% in simulated $t\bar{t}$ events, with a rejection factor for light-flavour jets of about 30 [61].

Selected events are required to have at least one vertex with at least two associated tracks with $p_T > 500$ MeV, and the primary vertex is selected to be the vertex reconstructed with the largest $\sum p_{\mathrm{T}}^2$ of its associated tracks.

A procedure to resolve overlap ambiguities is applied, as lepton and jet candidates can be reconstructed from the same detector information. In the $\ell^+\ell^-\ell'^+\ell'^-$ case, the overlap ambiguities are resolved as follows. If two electrons have overlapping energy deposits, the electron with the higher p_{T} is retained. If a reconstructed electron and muon share the same ID track, the muon is rejected if it is calorimeter-tagged; otherwise the electron is rejected. Reconstructed jets geometrically overlapping in a cone of size $\Delta R = 0.2$ with electrons or muons are also removed. The overlap removal in the $\ell^+\ell^-\nu\bar{\nu}$ case is similar to that in the $\ell^+\ell^-\ell'^+\ell'^-$ case, except for an additional criterion that removes any leptons close to the remaining jets with $0.2 < \Delta R < 0.4$. This additional criterion is not imposed in the $\ell^+\ell^-\ell'^+\ell'^-$ case due to the cleaner environment of this final state and in order to maximise the signal efficiency.

The missing transverse momentum $\vec{E}_{\mathrm{T}}^{\mathrm{miss}}$, which accounts for the imbalance of visible momenta in the plane transverse to the beam axis, is computed as the negative vector sum of the transverse momenta of all identified electrons, muons and jets, as well as a 'soft term', accounting for unclassified soft tracks and energy clusters in the calorimeters [62]. This analysis uses a track-based soft term, which is built by combining the information provided by the ID and the calorimeter, in order to minimise the effect of pile-up, which degrades the $\vec{E}_{\mathrm{T}}^{\mathrm{miss}}$ resolution.

5 Analysis of $\ell^+\ell^-\ell'^+\ell'^-$ final state

5.1 Event selection

Four-lepton events are selected and initially classified according to the lepton flavours: 4μ, $2e2\mu$, $4e$, called 'channels' hereafter. The selection is done using a combination of single lepton, dilepton, and trilepton trigger with separate transverse momentum thresholds. Due to an increasing peak luminosity, these p_{T} thresholds increased during the data-taking periods [63, 64]. For single-muon triggers, the p_{T} threshold increased from 20 GeV to 26 GeV, while for single-electron triggers, the p_{T} threshold increased from 24 GeV to 26 GeV. The overall trigger efficiency for signal events passing the final selection requirements is about 98%.

In each channel, four-lepton candidates are formed by selecting a lepton-quadruplet made out of two same-flavour, opposite-sign lepton pairs, selected as described in Section 4. Each electron (muon) is required to satisfy $p_T > 7$ (5) GeV and be in the pseudorapidity range of $|\eta| < 2.47$ (2.7). The highest-p_{T} lepton in the quadruplet must satisfy $p_T > 20$ GeV, and the second (third) lepton in p_{T} order must satisfy $p_T > 15$ GeV (10 GeV). In the case of muons, at most one calorimeter-tagged, segment-tagged or stand-alone ($2.5 < |\eta| < 2.7$) muon is allowed per quadruplet.

If there is ambiguity in assigning leptons to a pair, only one quadruplet per channel is selected by keeping the quadruplet with the invariant mass of the lepton pairs closest (leading pair) and second closest (subleading pair) to the Z boson mass, with invariant masses referred to as m_{12} and m_{34} respectively. In the selected quadruplet, m_{12} must satisfy $50 < m_{12} < 106$ GeV and m_{34} must satisfy $50 < m_{34} < 115$ GeV.

Selected quadruplets are required to have their leptons separated from each other by $\Delta R > 0.1$. For the 4μ and $4e$ quadruplets, if an opposite-charge same-flavour lepton pair is found with $m_{\ell\ell}$ below 5 GeV, the quadruplet is removed to suppress the contamination from J/ψ mesons. If multiple quadruplets from different channels are selected at this point, only the quadruplet from the channel with the highest signal acceptance is kept, in the order: 4μ, $2e2\mu$, $4e$.

The Z+jets and $t\bar{t}$ background contributions are reduced by imposing impact-parameter requirements as well as track- and calorimeter-based isolation requirements on the leptons. The sum of the track isolation and 40% of the calorimeter isolation is required to be less than 16% of the lepton p_{T}. The pile-up dependence of this isolation selection is reduced as compared to that of the previous search by optimising the criteria used for exclusion of tracks associated with a vertex other than the primary vertex and by the removal of topological clusters associated with tracks.

An additional requirement based on a vertex-reconstruction algorithm, which fits the four-lepton candidates with the constraint that they originate from a common vertex, is applied in order to further reduce the Z+jets and $t\bar{t}$ background contributions. A cut of $\chi^2/N_{\mathrm{dof}} < 6$ for 4μ and < 9 for the other channels is applied, with an efficiency larger than 99% for signal in all channels.

Some of the final-state-radiation (FSR) photons can be identified in the calorimeter and incorporated into the $\ell^+\ell^-\ell'^+\ell'^-$ analysis. The strategy to include FSR photons into the reconstruction of Z bosons is the same as in Run 1 [65]. After the FSR correction, the four-momenta of both dilepton pairs are recomputed by means of a Z-mass-constrained kinematic fit [66]. The Z-mass constraint is applied to both Z candidates. Events that pass this selection and are not yet split according to lepton flavours, form a category which is called 'inclusive' hereafter.

5.2 Event categorization

After this initial four-lepton event selection, events are further split into several categories, in order to probe different signal production modes, such as VBF production and ggF production [9]. To enhance the search sensitivity to the NWA signals, multivariate classifiers are optimised for the event categorisation as described in Section 5.2.1. In order to also obtain results that are more model-independent (since the training of the multivariate classifiers is usually based on a specific signal model), a cut-based event categorisation that increases the sensitivity in the VBF production mode is also considered and is described in Section 5.2.2. The search for LWA signals, due to the complexity of modelling the categorisation of the interference between heavy Higgs boson and SM Higgs boson processes, uses only the ggF-enriched categories of the cut-based analysis. The same strategy is adopted in the search for a Kaluza-Klein graviton excitation .

5.2.1 Multivariate analysis

In order to improve the sensitivity in the search for an NWA Higgs boson signal produced either in the VBF or the ggF production mode, two multivariate classifiers, namely a 'VBF classifier' and a 'ggF classifier', are used . These classifiers are built with deep neural networks (DNN) and use a architecture similar to that in [67], combining a multilayer perceptron (MLP) and one or two recurrent neural networks(rNN) [68]. For both classifiers, the outputs of the MLP and rNN(s) are combined and fed into an additional MLP that produces an event score.

The 'VBF classifier' uses two rNNs and an MLP. The two rNNs have as inputs the p_{T}-ordered transverse momenta and the pseudorapidities of the two leading jets, and the transverse momenta and the pseudorapidities of the four leptons in the event, respectively. The MLP uses as inputs the invariant mass of the four-lepton system, the invariant mass and the transverse momentum of the two-leading-jets system, the difference in pseudorapidity between the $\ell^+\ell^-\ell'^+\ell'^-$ system and the leading jet, and the minimum angular separation between the $\ell^+\ell^-$ or $\ell'^+\ell'^-$ pair and a jet.

The 'ggF classifier' uses one rNN and an MLP. The rNN has as inputs the p_{T}-ordered transverse momenta and the pseudorapidities of the four leptons in the event. The MLP uses as inputs the following variables: 1) the four-lepton invariant mass; 2) the transverse momentum and the pseudorapidity of the four-lepton system; 3) the production angle of the leading Z defined in the four-lepton rest frame, $cos\Theta^*$; 4) the angle between the negative final-state lepton and the direction of flight of leading (subleading) Z in the Z rest frame, $cos\Theta_1$ ($cos\Theta_2$); 5) the angle between the decay planes of the four final-state leptons expressed in the four-lepton rest frame, Φ; and 6) the transverse momentum and the pseudorapidity of the leading jet.

The two classifiers are trained separately using the above-listed discriminating variables on all simulated NWA signal events from their corresponding production mode, and the SM ZZ background events. The 'VBF classifier' is trained on events with at least two jets while the 'ggF classifier' is trained on events with fewer than two jets. Figure 1 shows the 'ggF classifier' and 'VBF classifier' output for the data, the SM background and an example signal with m_H = 600 GeV.

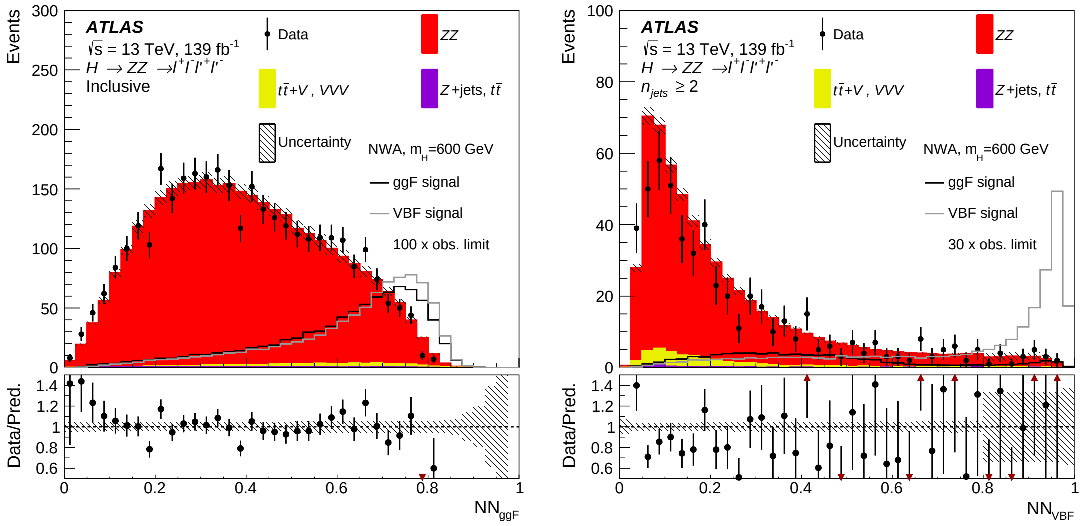

(a) (b)

Figure 1: The output of (a) the "ggF classifier" and (b) the 'VBF classifier' for the events passing the common event selections for the data, the SM background and NWA signal events with a mass of 600 GeV. For (b) the 'VBF classifier' output, an additional requirement of at least two jets in the event, is applied. The signal cross section is set to 100 times the observed limit for the 'ggF classifier' and 30 times the observed limit for the 'VBF classifier'. The ZZ background is scaled by the normalisation factors shown in Table 2. The lower panels show the ratio of data to prediction. Only statistical and experimental systematic uncertainties are included [9].

After the common event selection, as described in Section 5.1, events with at least two jets ($n_{jets} \geq 2$) and a 'VBF classifier' score value greater than 0.8 form the VBF-MVA-enriched category. Events failing to enter the VBF-MVA-enriched category are classified into the ggF-MVA-high category if the 'ggF classifier' score value is greater than 0.5; these events are further split into three distinct categories according to the lepton flavour of the $\ell^+\ell^-\ell'^+\ell'^-$ system. Finally, events failing both classifiers form the ggF-low category. Overall, five mutually exclusive categories are formed: VBF-MVA-enriched, ggF-MVA-high-4μ, ggF-MVA-high-2e2μ, ggF-MVA-high-4e, ggF-MVA-low. This categorisation is used in the search for a heavy scalar with the NWA and in the search in the context of a CP-conserving 2HDM.

The signal acceptance, defined as the ratio of the number of reconstructed events after all selection requirements to the total number of simulated events, is found to be between 30% (15%) and 46% (22%) in the ggF (VBF)-enriched category for the ggF (VBF) production mode depending on the signal mass hypothesis.

5.2.2 Cut-based analysis

In parallel a cut-based analysis is also performed to probe the sensitivity in the VBF production mode. If an event has two or more jets with p_{T} greater than 30 GeV, with the two leading jets being well separated in η, $\Delta\eta_{jj} > 3.3$, and having an invariant mass $m_{jj} > 400$ GeV, this event is classified into the VBF-enriched category; otherwise the event is classified into one of the ggF-enriched categories further split according to the lepton flavour of the $\ell^+\ell^-\ell'^+\ell'^-$ system. Four distinct categories are formed, namely

VBF-CBA-enriched, ggF-CBA-4μ, ggF-CBA-2e2μ, and ggF-CBA-4e. The ggF-enriched categories are used in the search for a heavy large-width scalar and the search for a Kaluza–Klein graviton excitation.

5.3 Background estimation

The main background source in the $H \to ZZ \to \ell^+\ell^-\ell'^+\ell'^-$ final state is non-resonant SM ZZ production (irreducible background), accounting for 97% of the total background events in the inclusive category. It arises from quark–antiquark annihilation $q\bar{q} \to ZZ$ (86%), gluon-initiated production $gg \to ZZ$ (10%), and a small contribution from EW vector-boson scattering (1%). The last of these is more important in the VBF-enriched category using the DNN-based categorisation, where it accounts for 20% of the total background events. While in the previous publication [10] the SM ZZ background was exclusively estimated from simulation for both the shape and the normalisation, in this analysis [9] its normalisation is derived from the data in the likelihood fit used in the statistical treatment of the data as explained in Section 9. The shapes of the $q\bar{q} \to ZZ$ and $gg \to ZZ$ invariant mass distributions are parameterised with analytic functions as described in Section 5.4

Additional background from the Z+jets and $t\bar{t}$ processes (reducible background) contribute to the total background yields only at the percent level and decrease more rapidly than the non-resonant ZZ contribution as a function of $m_{4\ell}$. These backgrounds are estimated using data where possible, following slightly different approaches for final states with a dimuon ($\ell\ell + \mu\mu$) or a dielectron ($\ell\ell + ee$) subleading pair [9, 69, 70].

The $\ell\ell + \mu\mu$ non-ZZ background includes mostly $t\bar{t}$ and Z+jets events, where in the latter case the muons arise mostly from heavy-flavour semileptonic decays and to a lesser extent from π/K in-flight decays. The main non-prompt background for the $\ell\ell + ee$ process arises from three sources: light-flavour jets misidentified as electrons; photon conversions; and semileptonic decays of heavy-flavour hadrons. The WZ production process is included in the data-driven estimates for the $\ell\ell + ee$ final states, while it is added from simulation for the $\ell\ell + \mu\mu$ final states even though its contribution to the total background is at the per-mill level. The contributions from $t\bar{t}V$ (where V stands for either a W or a Z boson) and triboson processes are minor and taken from simulated samples.

5.4 Signal modelling

The reconstructed four-lepton invariant mass $m_{4\ell}$ distribution is used as the discriminating variable for the $\ell^+\ell^-\ell'^+\ell'^-$ final state. It is extracted from the simulation of signal events and for most background components, except for the light-flavour jets and photon conversions in the case of $\ell\ell + ee$ background, which are taken from the control region as described in Section 5.3. To obtain statistical interpretations for each mass hypothesis, the $m_{4\ell}$ distribution for signal is parameterized as a function of the mass hypothesis m_H [9]. In the case of a narrow resonance, the width in $m_{4\ell}$ is determined by the detector resolution, which is modelled by the sum of a Crystal Ball (C) function [71, 72] and a Gaussian ($\mathcal{G}$) function:

$$P_s(m_{4\ell}) = f_C \times C(m_{4\ell}; \mu, \sigma_C, \alpha_C, n_C) + (1 - f_C) \times \mathcal{G}(m_{4\ell}; \mu, \sigma_{\mathcal{G}}).$$

The Crystal Ball and Gaussian functions share the same peak value of $m_{4\ell}$ (μ), but have different resolution parameters, σ_C and σ_G. The α_C and n_C parameters control the shape and position of the non-Gaussian tail, and the parameter f_C ensures the relative normalisation of the two probability density functions. To

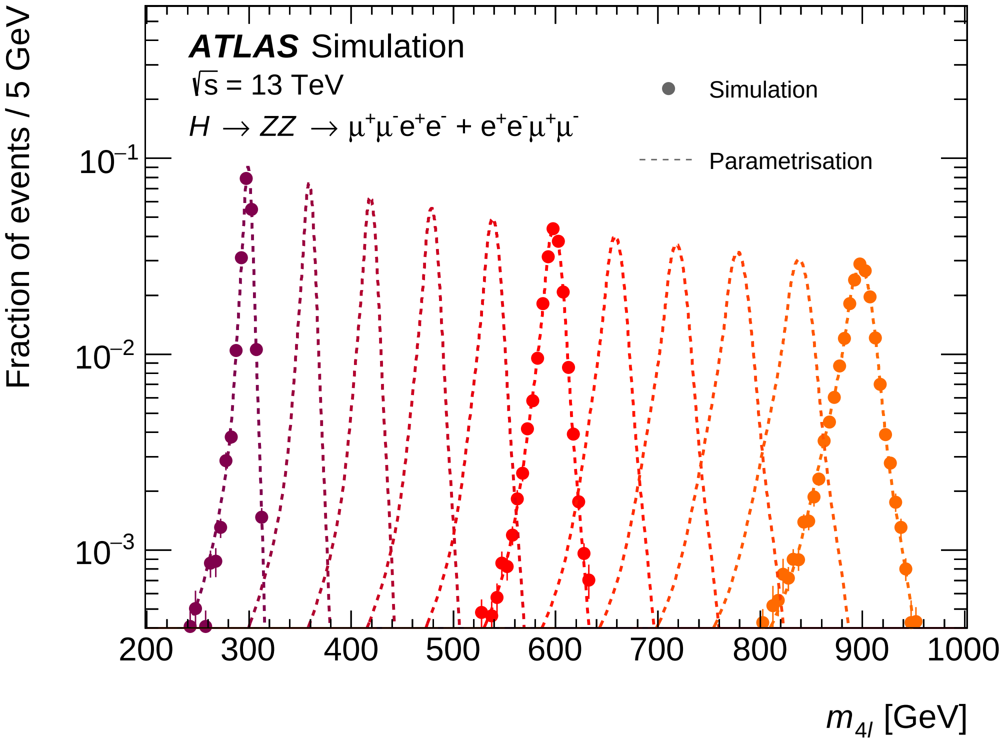

Figure 2: Parameterisation of the four-lepton invariant mass ($m_{4\ell}$) spectrum for various resonance mass (m_H) hypotheses in the NWA. Markers show the simulated $m_{4\ell}$ distribution for three specific values of m_H (300, 600, 900 GeV), normalised to unit area, and the dashed lines show the parameterisation used in the $2e2\mu$ channel for these mass points as well as for intervening ones [10].

improve the stability of the parameterisation in the full mass range considered, the parameter n_C is set to a fixed value. The bias in the extraction of signal yields introduced by using the analytic function is below 2% and treated as a systematic uncertainty of the signal parameterisation. The function parameters are determined separately for each final state using the simulated events for each generated mass m_H, and then fitted with a polynomial in m_H to interpolate between the generated mass points. The order of the polynomial is determined by first fitting with a third-order polynomial and then decreasing its order until the χ^2 is three times larger than the number of degrees of freedom. The use of this parameterisation for the function parameters introduces a bias in the signal yield and m_H extraction of about 1%. The extra bias is included in the systematic uncertainties of the signal acceptance. Example of signal parametrization is shown in Figure 2 [10] .

5.5 Background modelling

In the case of the LWA and the graviton model, a parton-level lineshape of $m_{4\ell}$ is derived from a theoretical calculation and multiplied by the signal acceptance obtained from the simulated events; it is then convolved with the detector resolution, using the same functions as those for modelling the narrow resonance [9]. The parton-level lineshape of $m_{4\ell}$ is taken from Ref. [75] for the LWA, and from Ref. [73] for the gravity model.

For the ZZ continuum background, the $m_{4\ell}$ distribution is parameterised by an empirical function for both the quark- and gluon-initiated processes in order to reduce the statistical uncertainties stemming from the limited number of simulated events. The empirical function is described by the following:

$$f_{qqZZ/ggZZ}(m_{4\ell}) = C_0 \times H(m_0 - m_{4\ell}) \times f_1(m_{4\ell}) + H(m_{4\ell} - m_0) \times f_2(m_{4\ell}),$$

where,

$$\begin{aligned} f_1(m_{4\ell}) &= \left(\frac{m_{4\ell} - a_4}{a_3}\right)^{a_1 - 1}\left(1 + \frac{m_{4\ell} - a_4}{a_3}\right)^{-a_1 - a_2}, \\ f_2(m_{4\ell}) &= \exp\left[b_0\left(\frac{m_{4\ell} - b_4}{b_3}\right)^{b_1 - 1}\left(1 + \frac{m_{4\ell} - b_4}{b_3}\right)^{-b_1 - b_2}\right], \\ C_0 &= \frac{f_2(m_0)}{f_1(m_0)}. \end{aligned}$$

The function's first part, f_1, covers the low-mass part of the spectrum until the ZZ threshold around $2m_Z$, and the second part, f_2, describes the high-mass tail. The transition between low- and high-mass parts is modelled with the Heaviside step function $H(x)$ around $m_0 = 260$ GeV for $q\bar{q} \rightarrow ZZ$ and around 350 GeV for $gg \rightarrow ZZ$. The continuity of the function around m_0 is ensured by the normalisation factor C_0 that is applied to the low-mass part. Finally, a_i and b_i are shape parameters which are obtained by fitting the $m_{4\ell}$ distribution in simulation for each category. A large number of $m_{4\ell}$ distributions are calculated from the analytic function with variations of the a_i and b_i values sampled from a multivariate Gaussian distribution that is constructed from their covariance matrix. The uncertainty in the $m_{4\ell}$ distribution is determined by calculating a central interval that captures 68% of the variations and is treated as a nuisance parameter in the likelihood fit, namely a ZZ parameterisation uncertainty. The ZZ parameterisation uncertainty is one of the leading systematic uncertainties for a low-mass signal.

5.6 Interference modeling

The gluon-initiated production of a heavy scalar H, the SM Higgs h and the $gg \rightarrow ZZ$ continuum background all share the same initial and final state, and thus lead to interference terms in the total amplitude [9]. Theoretical calculations [74] have shown that the effect of interference could modify the integrated cross section by up to $O(10\%)$, and this effect is enhanced as the width of the heavy scalar increases. Therefore, a search for a heavy scalar Higgs boson in the LWA case must properly account for two interference effects: the interference between the heavy scalar and the SM Higgs boson (denoted by $H - h$) and between the heavy scalar and the $gg \rightarrow ZZ$ continuum (denoted by $H - B$). However, because the width of the KK excitation resonance is relatively small, the interference effect is assumed to be negligible in the graviton interpretation for both final states. If the H and h bosons have similar properties, they have the same production and decay amplitudes and therefore the only difference between the signal and interference terms in the production cross section comes from the propagator. Hence, the acceptance and resolution of the signal and interference terms are expected to be the same. The $H - h$ interference is obtained by reweighting the particle-level lineshape of generated signal events using the following formula:

$$w(m_{4\ell}) = \frac{2 \cdot Re\left[\frac{1}{s - s_H} \cdot \frac{1}{(s - s_h)^*}\right]}{\frac{1}{|s - s_H|^2}},$$

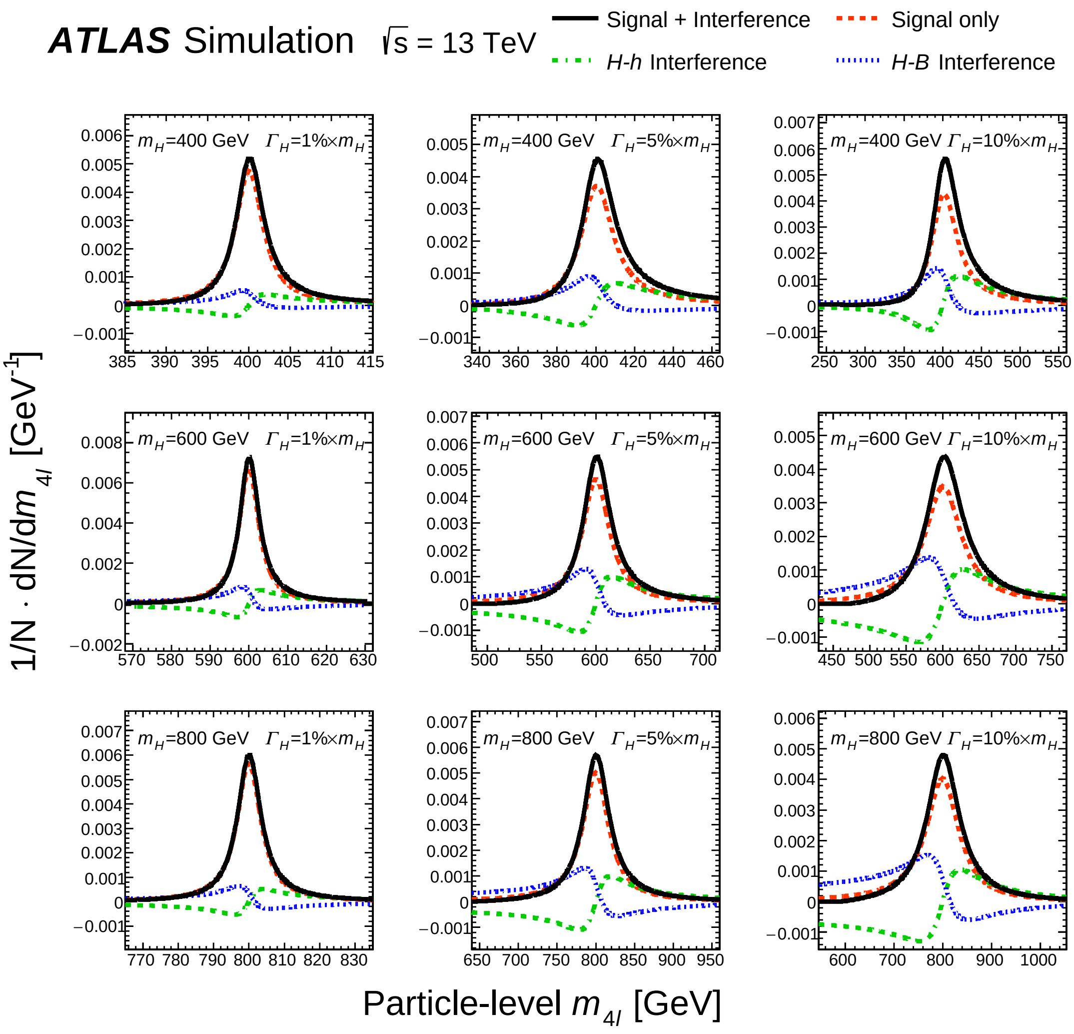

Figure 3: Particle-level four-lepton mass $m_{4\ell}$ model for signal only (red), H–h interference (green), H–B interference (blue) and the sum of the three processes (black). Three values of the resonance mass m_H (400, 600, 800 GeV) are chosen, as well as three values of the resonance width Γ_H (1%, 5%, 10% of m_H). The signal cross section, which determines the relative contribution of the signal and interference, is taken to be the cross section of the expected limit for each combination of m_H and Γ_H. The full model (black) is finally normalised to unity and the other contributions are scaled accordingly [10].

where $1/\left(s - s_{H(h)}\right)$ is the propagator for a scalar (H or h).

The particle-level lineshape is then convolved with the detector resolution function, the signal and interference acceptances are assumed to be the same. In order to extract the $H - B$ interference contribution, signal-only and background-only samples are subtracted from the generated SBI samples. The extracted particle-level $m_{4\ell}$ distribution for the $H - B$ interference term is then convolved with the detector resolution. An example of LWA signal plus interference parameterization modelling is shown in Figure 3 [10].

6 Analysis of $\ell^+\ell^-\nu\bar{\nu}$ final state

6.1 Event selection and categorisation

The $\ell^+\ell^-\nu\bar{\nu}$ final state consists of a pair of high-p_T isolated leptons (electrons or muons) and large E_T^{miss} and is subject to larger background contamination than the $\ell^+\ell^-\ell'^+\ell'^-$ channel [9].

Events are recorded using a combination of multiple single-lepton triggers, resulting in a high efficiency of about 98% for typical signal processes in the signal region. These candidate events are preselected by requiring exactly two electrons or muons with opposite charges and $p_T > 20$ GeV, where the electrons (muons) must have $|\eta| < 2.47$ (2.5). The leading lepton is further required to have $p_T > 30$ GeV, well above the threshold of the single-lepton triggers. The selected electrons or muons must have a longitudinal impact parameter satisfying $|z_0 sin(\Theta)| < 0.5$ mm. The lepton candidates are required to satisfy the same isolation criteria and the same requirement on the transverse impact-parameter significance as used in the $\ell^+\ell^-\ell'^+\ell'^-$ channel (see Section 5.1), resulting in an efficiency above 98% for typical prompt leptons with $p_T > 30$ GeV. To suppress the WZ background, events containing any additional lepton satisfying the 'loose' identification requirement with $p_T > 7$ GeV, in addition to the other requirements, are rejected. Requiring the dilepton invariant mass ($m_{\ell\ell}$) to be between 76 and 106 GeV largely reduces the contamination from the non-resonant-$\ell\ell$ background, originating from $t\bar{t}$, Wt, WW, and $Z \to t\bar{t}$ production. The data sample after the preselection is dominated by the Z+jets and the remaining non-resonant-$\ell\ell$ processes. To suppress these backgrounds, a further selection based on E_T^{miss} and event topology is applied.

In addition, candidate events are required to have E_T^{miss}>120 GeV, which suppresses the Z+jets contamination by several orders of magnitude. The number of residual $Z + jets$ events, which have large fake E_T^{miss}, is further reduced by requiring S(E_T^{miss})>10, where S(E_T^{miss}) is the statistical significance of the E_T^{miss} value against the null hypothesis of zero-E_T^{miss} [75]. Additional selection criteria based on angular variables are imposed to further reject the Z+jets and non-resonant-$\ell\ell$ background events [9]. After these cuts, the Z+jets process only constitutes a small fraction of the total background (about 4%). Finally, events containing one or more b-jets are vetoed to further suppress the $t\bar{t}$ and Wt backgrounds.

The signal region for the VBF production mode (VBF-enriched signal region) is defined for candidate events containing at least two selected jets with $p_T > 30$ GeV, where the two leading jets must have $m_{jj} > 550$ GeV and $\Delta\eta_{jj} > 4.4$. The remaining events, failing the requirements for the VBF-enriched signal region, are categorised for the ggF-enriched signal region. The signal acceptance in the ggF-enriched signal region for signal events containing a heavy spin-0 resonance from ggF production is about 30% at $m_H = 400$ GeV and up to 50% at $m_H = 1.4$ TeV. For VBF signal events the signal acceptance in the VBF-enriched signal region is generally lower, ranging from 3% at $m_H = 400$ GeV to 20% at $m_H = 1.6$ TeV.

6.2 Background estimation

In the ggF-enriched signal region, the major backgrounds originate from the ZZ and WZ processes, which account for 60% and 30% of the total background contribution, respectively. The non-resonant-$\ell\ell$ background yields a relative contribution of about 5% to the total background, while the largely suppressed Z+jets background contribute about 4%. The remaining contributions from other processes (VVV and $t\bar{t}V$), amount in total to less than 1% of the total background. A similar composition of background processes is found in the VBF-enriched signal region, where the total background yield is expected to be smaller than 1% of that in the ggF-enriched signal region, due to the event selection for the VBF phase space [9].

The main background contribution from ZZ production is estimated using a semi-data-driven method. Similar to the $\ell^+\ell^-\ell'^+\ell'^-$ analysis, the predicted ZZ yield is scaled by a floating normalisation factor, which is determined in the statistical fit to the signal-region data (see Section 8.1). The introduction of the data-driven normalisation factor helps to constrain the total uncertainty in the ZZ yield, while the theoretical and experimental uncertainties in the transverse mass distribution are evaluated from simulation.

To estimate the background from WZ production in the ggF-enriched signal region, a control region enriched in WZ events, with a purity of over 90%, is defined using the preselection criteria, except that a third lepton with $p_T > 20$ GeV is required. Several further selections such as S(E_T^{miss})>3, a b-jets veto, and $m_T^W > 60$ GeV are applied to suppress non-WZ contributions [9, 76]. The total uncertainty in the WZ estimate for the ggF-enriched signal region is about 5%. A similar method is adopted to estimate the WZ contribution in the VBF-enriched signal region, additionally selecting two jets with $p_T > 30$ GeV for the control region [9, 77]. The total uncertainty in the WZ estimate for the VBF-enriched signal region is about 30%. The kinematic distributions are estimated from simulation.

To estimate the non-resonant-$\ell\ell$ background, a control region dominated by the non-resonant-$\ell\ell$ processes (with a purity of about 95%) is defined. For this, all the event selection criteria are used, except that the final state is required to contain an opposite-sign $e\mu$ pair. The total uncertainty in the non-resonant-$\ell\ell$ estimate in the ggF-enriched signal region is about 9%. The estimation of the non-resonant-$\ell\ell$ background in the VBF-enriched signal region relies on a similar methodology, where the control region is defined with a jet selection that is looser than in the signal region. The relative uncertainty in the final estimate in the VBF-enriched signal region is 70%. The kinematic distributions for the non-resonant-$\ell\ell$ background in the signal region are predicted with simulation, and the assigned systematic uncertainty covers the experimental uncertainty in the simulated shape as well as the difference between data and simulation in the control region.

The Z+jets background contribution is estimated from simulation and scaled by a normalisation factor derived in a control region enriched in Z+jets events. The control region is defined with all event selection criteria except that S(E_T^{miss}) must be less than 9. The total uncertainty in the Z+jets estimate is about 40%. The kinematic distributions for the Z+jets background are modelled with simulation. Finally, backgrounds from the VVV and $t\bar{t}V$ processes, which contribute less than 1% of the total background, are estimated from simulation.

6.3 Signal and background modelling

The modelling of the transverse mass m_T distribution for signal and background is based on templates derived from fully simulated events and afterwards used to fit the data [9]. For a narrow resonance, simulated events generated for fixed mass hypotheses as described in Section 3 are used as the inputs in the moment-morphing technique [78] to obtain the m_T distribution for any other mass hypothesis. The interference terms for the LWA case are extracted in the same way as in the $\ell^+\ell^-\ell'^+\ell'^-$ final state, as described in Section 5.6. In the case of the $\ell^+\ell^-\nu\bar{\nu}$ final state a correction factor, extracted as a function of m_{ZZ}, is used to reweight the interference distributions obtained at particle level to account for reconstruction effects. The final expected LWA m_T distribution is obtained from the combination of the interference distributions with simulated m_T distributions, which are interpolated between the simulated mass points with a weighting technique using the Higgs propagator, a method similar to that used for the interference.

7 Systematic uncertainties

The systematic uncertainties can be categorised into experimental and theoretical uncertainties [9]. The first category includes the uncertainties resulting from the integrated luminosity, the trigger efficiencies, the momentum scale and resolution of tracks, the reconstruction and identification of leptons and jets, and their energy scale and resolution calibrations. Systematic uncertainties associated with data-driven methods are also in this category but described in their corresponding sections: Section 5.3 for $\ell^+\ell^-\ell'^+\ell'^-$ final state and Section 6.2 for $\ell^+\ell^-\nu\bar{\nu}$ final state. The second category includes the uncertainties in the theoretical descriptions of the signal and background simulations. These systematic uncertainties evaluated separately for signal and background in each category affect signal acceptances and background yields as well as the probability density distributions of the discriminating variables. They are provided as the inputs for the statistical interpretations described in Section 8, where the impact of these uncertainties on the expected signal yields are presented.

7.1 Experimental uncertainties

The uncertainty in the combined 2015-2018 integrated luminosity is found to be 1.7% [79], obtained using the LUCID-2 detector [80] for the primary luminosity measurements. The lepton identification and reconstruction efficiency as well as the energy/momentum scale and resolution are derived from data using $J/\Psi \to \ell\ell$ and $Z \to \ell\ell$ decay events. The uncertainties in the reconstruction performance are computed for electrons [53] and for muons [54]. In general, their impact on the signal and background yields is less than 1% in the $\ell^+\ell^-\nu\bar{\nu}$ final state, and up to 1.5% in the $\ell^+\ell^-\ell'^+\ell'^-$ final state. In addition, the lepton isolation uncertainty is estimated to be less than 1% in both final states. The uncertainties in the jet energy scale and resolution have several sources, including uncertainties in the absolute and relative in situ calibration, the correction for pile-up, the flavour composition and response [81]. Each source is treated as an independent component. They vary from 4.5% for jets with transverse momentum $p_T = 20$ GeV, decreasing to 1% for jets with $p_T = 100 - 1500$ GeV and increasing again to 3% for jets with higher p_{T}. They are the dominant uncertainties in the VBF-enriched categories for ggF signal production and SM ZZ production in both final states. Uncertainties in the lepton and jet energy scales are propagated to the uncertainty in the E_T^{miss} [82]. In addition, the uncertainties from the momentum scale and resolution of the tracks that are not associated with any identified lepton or jet contribute 8% and 3%, respectively, to the uncertainty in the E_T^{miss} value. As the efficiency of the lepton triggers in events with reconstructed leptons is nearly 100%, the related uncertainties are negligible. The uncertainties associated with the pile-up reweighting are also taken into account; their impact on the signal and background yields is about 1% for both final states. These experimental uncertainties are common to the two final states; therefore, they are fully correlated between the two final states.

7.2 Theoretical uncertainties

For the simulation-based estimates, the theoretical uncertainties from parton distribution functions (PDFs), missing higher-order QCD corrections, and parton showering are considered. The PDF uncertainty is evaluated by taking the envelope of variations among alternative PDF choices and the estimate from its internal PDF error sets, following the PDF4LHC recommendation [83]. The missing higher-order QCD corrections are estimated by halving or doubling the factorisation and renormalization scales independently, among which the largest effect is taken as the systematic uncertainty. By varying the Pythia configurations, such as the parameter values of the AZNLO tune, the multi-parton models and the final-state radiation models, allows to assess the parton-showering uncertainty. For different signal hypotheses, the impact of these theoretical uncertainties on the signal acceptance and the spectrum of the discriminating variables is determined. In total, the theoretical uncertainty in the signal acceptance varies from less than 1% in the low mass region to 12% in the high mass region of the $\ell^+\ell^-\nu\bar{\nu}$ final state, and from less than 1% in the low mass region to up to 20% in the high mass region of the $\ell^+\ell^-\ell'^+\ell'^-$ final state. For the continuum ZZ background, a common floating normalisation factor is introduced to scale the number of events for the $q\bar{q} \to ZZ$ and $gg \to ZZ$ processes, while the relative yields of the two processes are estimated from the simulations. Therefore, in addition to the spectrum of the discriminating variables in the ZZ background, the theoretical uncertainties are also propagated to the simulation-based estimation of the relative yields. Moreover, the uncertainty associated with the NLO EW corrections, calculated in Refs. [35, 36, 38], are also taken into account, affecting the discriminating variables by less than 1% in the low mass region and up to 10% in the high mass region for both final states. As the $\ell^+\ell^-\ell'^+\ell'^-$ and $\ell^+\ell^-\nu\bar{\nu}$ searches are sensitive to different energy scales, these theoretical uncertainties are assumed to be completely uncorrelated between the two analyses.

8 Results

The statistical procedure used to extract the results is described in Section 8.1 and the general results are presented in Section 8.2 [9].

8.1 Statistical procedure

The statistical treatment of the data interpretation follows the procedure for the Higgs-boson search combination in 7 TeV data [84, 85]. The test statistic used for limit setting is the profile likelihood ratio $\Lambda(\alpha, \boldsymbol{\theta})$, which depends on one or more parameters of interest α, additional normalisation factors and extra nuisance parameters Θ. The parameter of interest is the cross-section times branching ratio of the heavy resonance decaying into the two final states. The normalisation factors, which were not used in the previous publication [10], are introduced separately for each final state to scale the expected number of the SM ZZ background events in each category [9]. They are determined by a likelihood fit to the data, allowing the systematic uncertainty to be reduced by removing both the theoretical and luminosity uncertainty contributing to the normalisation uncertainty. In the $\ell^+\ell^-\ell'^+\ell'^-$ final state, three floating normalisation factors are introduced for the VBF-enriched, ggF-MVA-high and ggF-MVA-low categories. They are referred to as μZZVBF-MVA, μZZggF-MVA-high and μZZggF-MVA-low, respectively. The use of three ZZ normalisation factors for the $\ell^+\ell^-\ell'^+\ell'^-$ final state is motivated by the different phase spaces defined for the respective signal regions. Due to the limited size of the data sample and the worse signal-to-background ratio in the respective VBF-enriched signal region, only one floating normalisation factor μ_{ZZ} is introduced in the $\ell^+\ell^-\nu\bar{\nu}$ final state.

The nuisance parameters represent the estimates of the systematic uncertainties and each of them is constrained by a Gaussian distribution. For each category of each final state, a discriminating variable is used to further separate signal from background. The statistical uncertainty of the data sample dominates in both of the present searches, and the systematic uncertainty impacts the searches to a much lesser extent. The number of signal events is extracted from a simultaneous fit to the discriminating variable, $m_{4\ell}$ in the $\ell^+\ell^-\ell'^+\ell'^-$ analysis and m_T in the $\ell^+\ell^-\nu\bar{\nu}$ analysis, in the event categories described in Sections 5 and 6.

Table 1: The ZZ normalisation factors together with their total uncertainties in each category of the two final states, which scale the number of ZZ events estimated from the simulations, obtained from a simultaneous likelihood fit of the two final states under the background-only hypothesis. For the $\ell^+\ell^-\ell'^+\ell'^-$ final state, the MVA-based categorisation is used [9].

Final state	Normalisation factor	Fitted value
$\ell^+\ell^-\ell'^+\ell'^-$	$\mu_{ZZ}^{\text{VBF-MVA}}$	0.9 ± 0.3
	$\mu_{ZZ}^{\text{ggF-MVA-high}}$	1.07 ± 0.05
	$\mu_{ZZ}^{\text{ggF-MVA-low}}$	1.12 ± 0.03
$\ell^+\ell^-\nu\bar{\nu}$	μ_{ZZ}	1.07 ± 0.05

Table 2: Expected and observed numbers of events in the $\ell^+\ell^-\ell'^+\ell'^-$ final state for $m_{4\ell} > 200$ GeV, together with their uncertainties, for the VBF-MVA-enriched, ggF-MVA-high and ggF-MVA-low categories. The expected numbers of events, as well as their uncertainties, are obtained from a combined likelihood fit to the data under the background-only hypothesis. The uncertainties of the ZZ normalisation factors, presented in Table 1, are also taken into account [9].

Process	VBF-enriched	ggF-MVA-high			ggF-MVA-low
		4μ channel	$2e2\mu$ channel	$4e$ channel	
$q\bar{q} \to ZZ$	11 ± 4	232 ± 10	389 ± 17	154 ± 7	2008 ± 47
$gg \to ZZ$	3 ± 2	37 ± 6	64 ± 10	26 ± 4	247 ± 19
ZZ (EW)	4.1 ± 0.4	4.5 ± 0.2	7.5 ± 0.4	3 ± 0.2	14.3 ± 0.7
Z + jets, $t\bar{t}$	0.08 ± 0.02	0.6 ± 0.1	1.7 ± 0.4	0.8 ± 0.1	8.8 ± 2.1
$t\bar{t}V$, VVV	0.97 ± 0.1	9.8 ± 0.2	17.5 ± 0.4	7.8 ± 0.2	21.9 ± 0.5
Total background	19 ± 5	284 ± 12	480 ± 20	192 ± 8	2300 ± 51
Observed	19	271	493	191	2301

8.2 General results

The total number of observed events is 3275 in the $\ell^+\ell^-\ell'^+\ell'^-$ final state ($m_{4\ell} > 200$ GeV) and 2883 in the $\ell^+\ell^-\nu\bar{\nu}$ final state. The expected background yields are obtained from a simultaneous likelihood fit of the two final states under the background-only hypothesis. Table 1 summarises the fitted normalisation factors for the SM ZZ background. The number of observed candidate events with mass above 200 GeV and the expected background yields for each of the five categories of the $\ell^+\ell^-\ell'^+\ell'^-$ analysis as described in Section 5.2, are presented in Table 2. The $m_{4\ell}$ spectrum in each category is shown in Figure 4. Table 3 contains the number of observed events along with the obtained background yields for the $\ell^+\ell^-\nu\bar{\nu}$ analysis. Figure 5 shows the m_T distribution for the electron and muon channels in the ggF-enriched and VBF-enriched categories. The maximum deviation of the data from the background-only hypothesis is evaluated in the context of a NWA signal from the ggF production or from the VBF production separately. For the ggF production, the maximum deviation is for a signal mass hypothesis around 240 GeV, with a local significance of 2.1σ and a global significance of 0.5σ. For the VBF production, the maximum deviation is for a signal mass hypothesis around 660 GeV, with a local significance of 2.6σ and a global significance of 1.2σ.

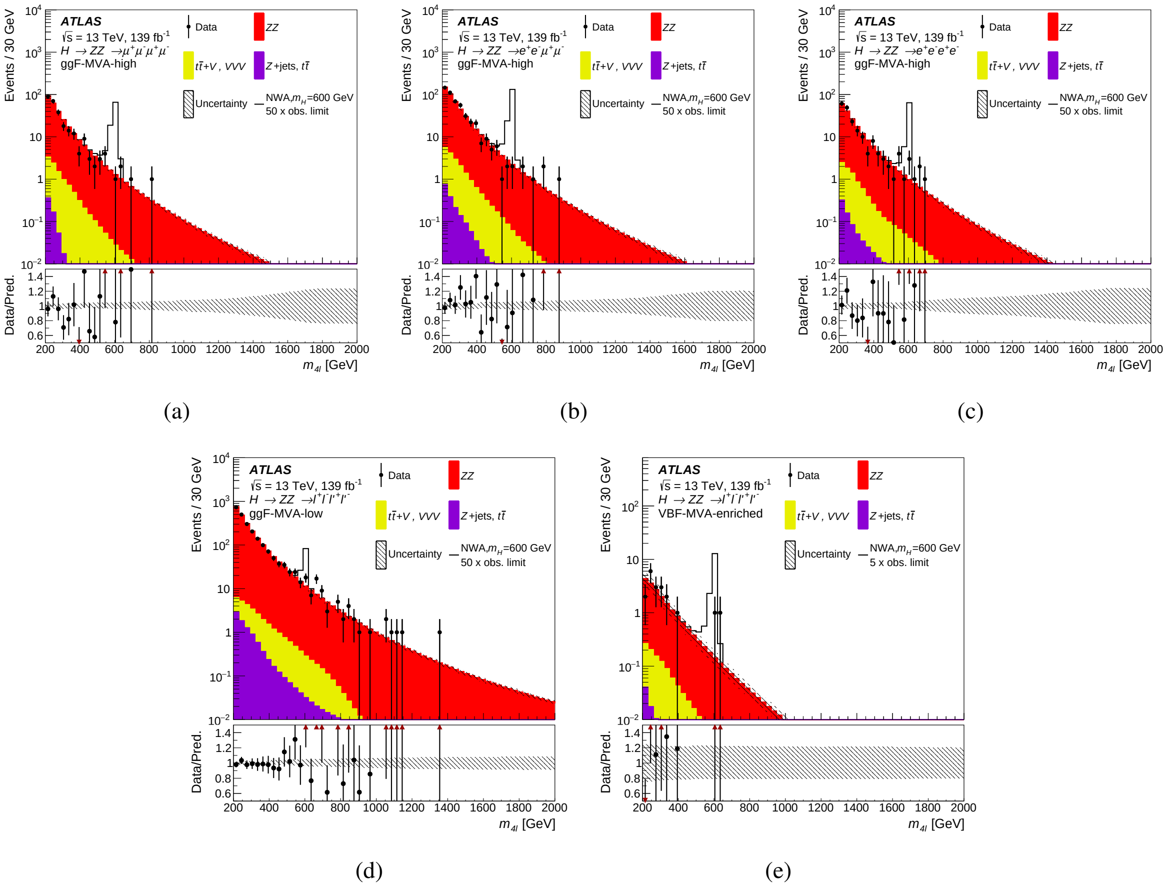

Figure 4: Distributions of the four-lepton invariant mass $m_{4\ell}$ in the $\ell^+\ell^-\ell'^+\ell'^-$ search for the ggF-MVA-high categories ($\mu^+\mu^-\mu^+\mu^-$ (a), $e^+e^-\mu^+\mu^-$ (b), and $e^+e^-e^+e^-$ (c) final states), for the ggF-MVA-low category (d), and for the VBF-MVA-enriched category (e). The backgrounds are determined from a combined likelihood fit to the data under the background-only hypothesis. The simulated m_H = 600 GeV signal is normalised to a cross section corresponding to 50 (5) times the observed limit given in Section 9.1.1 for the ggF (VBF) production mode. The error bars on the data points indicate the statistical uncertainty, while the systematic uncertainty in the prediction is shown by the hatched band. The lower panels show the ratio of data to prediction. The red arrows indicate data points that are outside the displayed range [9].

9 Interpretations

Since no significant excess with respect to the background predictions is found, the results obtained from the combination of the $\ell^+\ell^-\ell'^+\ell'^-$ and $\ell^+\ell^-\nu\bar{\nu}$ final states are interpreted in terms of exclusion limits for different signal hypotheses [9].

9.1 Spin-0 resonances

9.1.1 Spin-0 resonances with NWA

Upper limits on the cross-section times branching ratio ($\sigma \times B(H \rightarrow ZZ)$) for a heavy resonance are obtained as a function of m_H with the CL$_s$ procedure [86] in the asymptotic approximation from the combination of the two final states. The results were verified to be correct within about 4% using

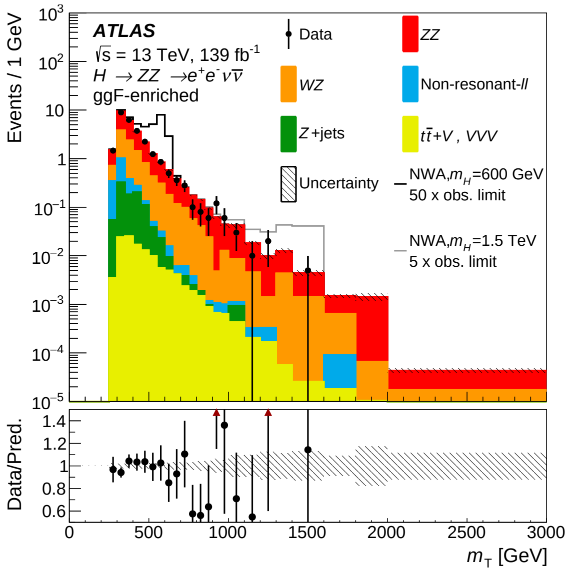

(a)

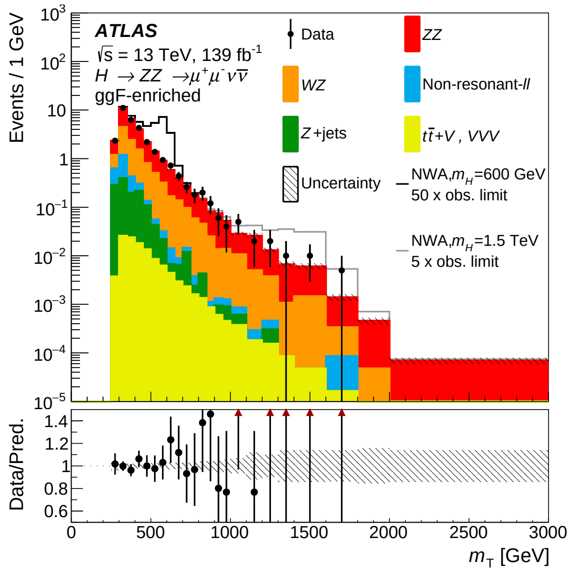

(b)

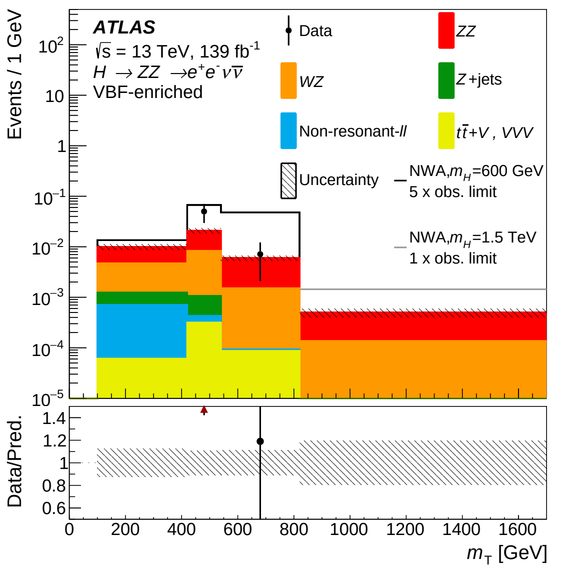

(c)

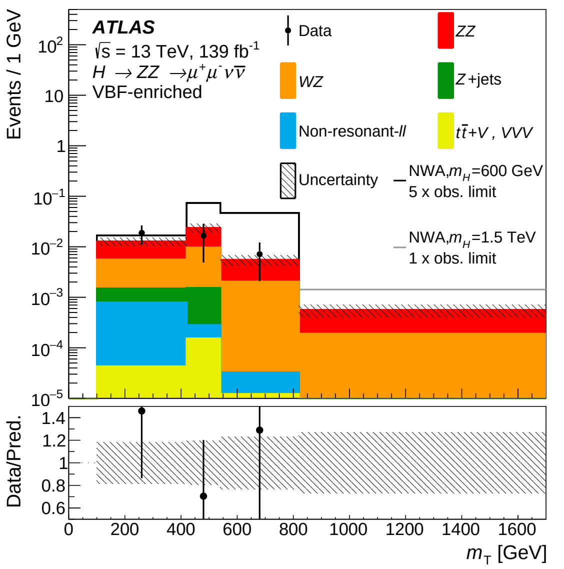

(d)

Figure 5: The m_T distribution in the $\ell^+\ell^-\nu\bar{\nu}$ search for (a),(b) the ggF categories and (c),(d) the VBF categories. Events beyond the upper limit of the histogram are included in the last bin of the distribution. The backgrounds are determined from a combined likelihood fit to data under the background-only hypothesis. The simulated m_H = 600 GeV (1.5 TeV) signals are normalised to a cross section corresponding to 50 (5) times the observed limit given in Section 9.1.1 for the ggF production mode and to 5 (1) times the observed limit for the VBF production mode. The error bars on the data points indicate the statistical uncertainty and markers are drawn at the bin centre. The systematic uncertainty in the prediction is shown by the hatched band. The lower panels show the ratio of data to prediction. The red arrows indicate data points that are outside the displayed range [9].

Table 3: Expected and observed numbers of events together with their uncertainties in the $\ell^+\ell^-\nu\bar{\nu}$ final state, for the ggF- and VBF-enriched categories. The expected numbers of events, as well as their uncertainties, are obtained from a likelihood fit to the data under the background-only hypothesis. The uncertainties of the ZZ normalisation factors, presented in Table 1, are also taken into account [9].

Process	ggF-enriched		VBF-enriched	
	e^+e^- channel	$\mu^+\mu^-$ channel	e^+e^- channel	$\mu^+\mu^-$ channel
$q\bar{q} \to ZZ$	714 ± 38	817 ± 44	2.9 ± 0.2	3.5 ± 0.2
$gg \to ZZ$	94 ± 29	105 ± 32	1 ± 0.5	1 ± 0.4
ZZ (EW)	6.6 ± 0.5	7 ± 0.5	0.8 ± 0.1	0.9 ± 0.1
WZ	412 ± 14	455 ± 12	2.5 ± 0.5	3 ± 1.5
Z + jets	43 ± 13	60 ± 22	0.3 ± 0.2	0.4 ± 0.3
Non-resonant-$\ell\ell$	66 ± 6	77 ± 7	0.2 ± 0.2	0.3 ± 0.2
$t\bar{t}V$, VVV	5.9 ± 0.4	5.9 ± 0.4	0.09 ± 0.02	0.04 ± 0.01
Total backgrounds	1342 ± 52	1527 ± 60	7.8 ± 0.8	9 ± 1.6
Observed	1323	1542	8	10

pseudo-experiments. It is assumed that an additional heavy scalar would be produced mainly via the ggF and VBF processes but that the ratio of the two production mechanisms might depend on the model considered. Therefore, fits for the ggF and VBF processes are done separately, in each case the other process is allowed to float in the fit as an additional free parameter. Figure 6 presents the observed and expected limits at 95% CL on the $\sigma \times B(H \to ZZ)$ of a narrow scalar resonance for the ggF (left) and VBF (right) production modes, as well as the expected limits from the $\ell^+\ell^-\ell'^+\ell'^-$ and $\ell^+\ell^-\nu\bar{\nu}$ searches. This result is valid for models in which the width is less than 0.5% of m_H . Combining the two final states, the 95% CL upper limits range from 200 fb at m_H = 240 GeV to 2.6 fb at m_H = 2000 GeV for the ggF production mode and from 87 fb at m_H = 250 GeV to 1.9 fb at m_H = 1800 GeV for the VBF production mode. Compared with the results projected to the luminosity of 139 fb^{-1} from the previous publication [10], the results are improved by a factor ranging from 9% to 23% for the ggF production mode and from 23% to 38% for the VBF production mode, depending on the mass hypothesis [9].

9.1.2 Spin-0 resonances with LWA

In the case of LWA, upper limits on the cross section for the ggF process times branching ratio ($\sigma_{\text{ggF}} \times B(H \to ZZ)$) are set for different widths of the heavy scalar. Figure 7 shows the limits for a width of 1%, 5%, 10% and 15% of m_H respectively. The limits are set for masses of m_H higher than 400 GeV.

9.1.3 Two-Higgs Doublet Model (2HDM)

A search in the context of a CP-conserving 2HDM is also presented. This model has five physical Higgs Bosons after electroweak symmetry breaking: two CP-even, one CP-odd, and two charged. The model considered here has seven free parameters: the Higgs boson masses, the ratio of the vacuum expectation values of the two Higgs doublets ($\tan\beta$), the mixing angle between the CP-even Higgs bosons (α), and the potential parameter m_{12}^2 that mixes the two Higgs doublets. The two Higgs doublets $\Phi 1$ and $\Phi 2$ can couple to leptons and up- and down-type quarks in several ways. In the Type-I model, $\Phi 2$ couples to all quarks

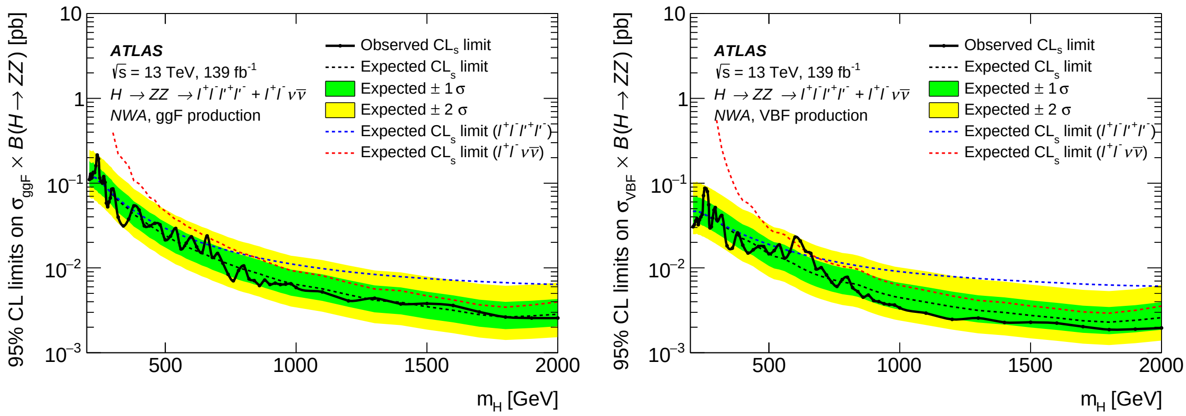

(a) (b)

Figure 6: The upper limits at 95% CL on the cross section times branching ratio as a function of the heavy resonance mass m_H for (a) the ggF production mode ($\sigma_{\text{ggF}} \times B(H \to ZZ)$) and (b) for the VBF production mode ($\sigma_{\text{VBF}} \times B(H \to ZZ)$) in the case of the NWA. The black line indicates the observed limit. The green and yellow bands represent the $\pm 1\sigma$ and $\pm 2\sigma$ uncertainties in the expected limits. The dashed coloured lines indicate the expected limits obtained from the individual searches [9].

and leptons, whereas for Type-II, $\Phi1$ couples to down-type quarks and leptons and $\Phi2$ couples to up-type quarks. The 'lepton-specific' model is similar to Type-I except for the fact that the leptons couple to $\Phi1$, instead of $\Phi2$; the 'flipped' model is similar to Type-II except that the leptons couple to $\Phi2$, instead of $\Phi1$. In all these models, the coupling of the heavier CP-even Higgs boson to vector bosons is proportional to $\cos(\beta - \alpha)$. In the limit $\cos(\beta - \alpha) \to 0$, the light CP-even Higgs boson is indistinguishable from a SM Higgs boson with the same mass. In the context of $H \to ZZ$ decays there is no direct coupling of the Higgs boson to leptons, so only the Type-I and II interpretations are presented. In addition, our interpretations assume other Higgs bosons are heavy enough so that the heavy CP-even Higgs boson will not decay to them. Figure 8 shows exclusion limits in the $\tan\beta$ versus $\cos(\beta - \alpha)$ plane for Type-I and Type-II 2HDMs, for a heavy Higgs boson with mass $m_H = 220$ GeV. This m_H value is chosen so that the assumption of a narrow Higgs boson is valid over most of the parameter space, and the experimental sensitivity is maximal. At this low mass, only the $\ell^+\ell^-\ell'^+\ell'^-$ final state contributes to this result. The range of $\cos(\beta - \alpha)$ and $\tan\beta$ explored is limited to the region where the assumption of a heavy narrow Higgs boson with negligible interference is valid. When calculating the limits at a given choice of $\cos(\beta - \alpha)$ and $\tan\beta$, the relative rates of ggF and VBF production in the fit are set to the prediction of the 2HDM for that parameter choice. Figure 9 shows exclusion limits as a function of the heavy Higgs boson mass m_H and the parameter $\tan\beta$ for $\cos(\beta - \alpha) = -0.1$, which is chosen so that the light Higgs boson properties are still compatible with the recent measurements of the SM Higgs boson properties [87]. The white regions in the exclusion plots indicate regions of parameter space which are not excluded by the present analysis. In these regions the cross section predicted by the 2HDM is below the observed cross-section limit. In comparison with the previous publication [10], the excluded regions are significantly expanded [9]. For example, in the $\tan\beta$ versus m_H plane for the Type-II 2HDM the excluded region in $\tan\beta$ is more than 60% larger for $200 < m_H < 400$ GeV

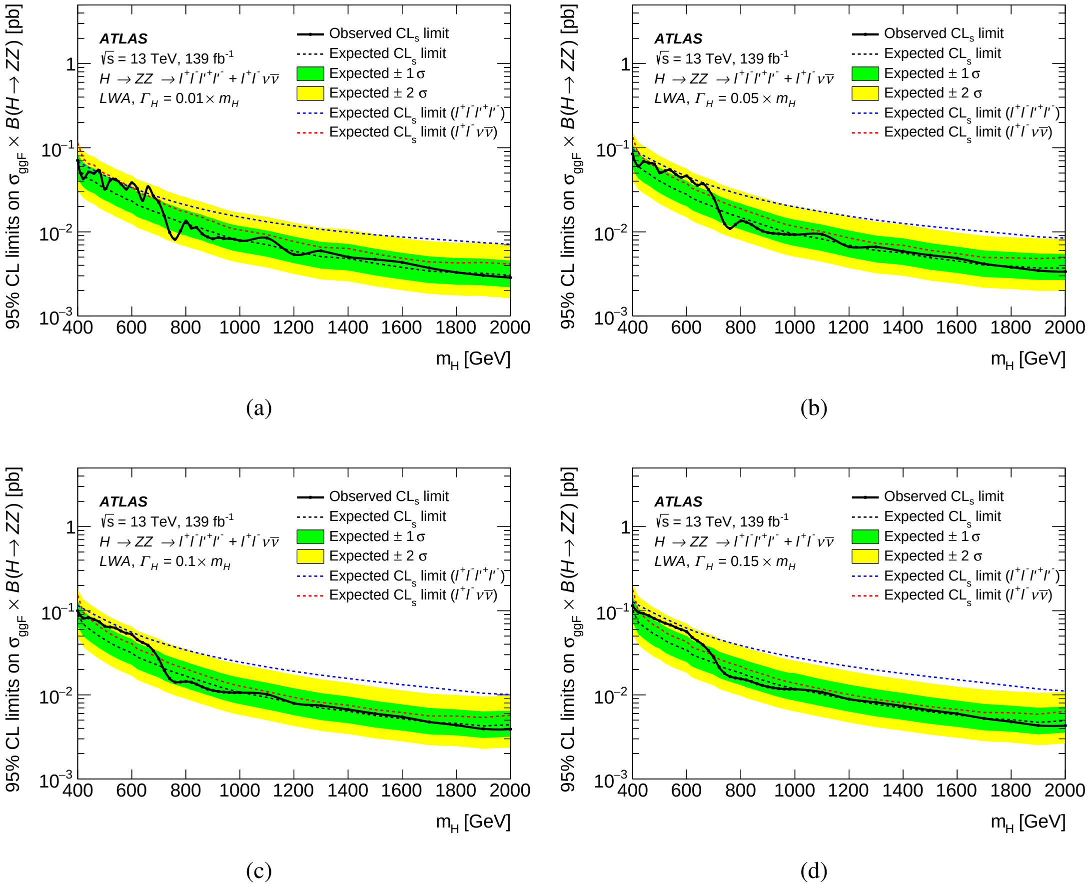

Figure 7: The upper limits at 95% CL on the cross section for the ggF production mode times branching ratio ($\sigma_{\text{ggF}} \times B(H \to ZZ)$) as a function of m_H for an additional heavy scalar assuming a width of (a) 1%, (b) 5%, (c) 10% and (d) 15%, of m_H. The black line indicates the observed limit. The green and yellow bands represent the $\pm 1\sigma$ and $\pm 2\sigma$ uncertainties in the expected limits. The dashed coloured lines indicate the expected limits obtained from the individual searches [9].

9.2 Spin-2 resonances

The results are also interpreted as a search for a Kaluza-Klein graviton excitation, G_{KK}, in the context of the bulk RS model with $k/\bar{M}_{Pl} = 1$. The limits on $\sigma \times B(G_{KK} \to ZZ)$ at 95% CL as a function of the KK graviton mass, $m(G_{KK})$, are shown in Figure 10 together with the predicted G_{KK} cross section. A spin-2 graviton can clearly be excluded up to a mass of 1750 GeV.

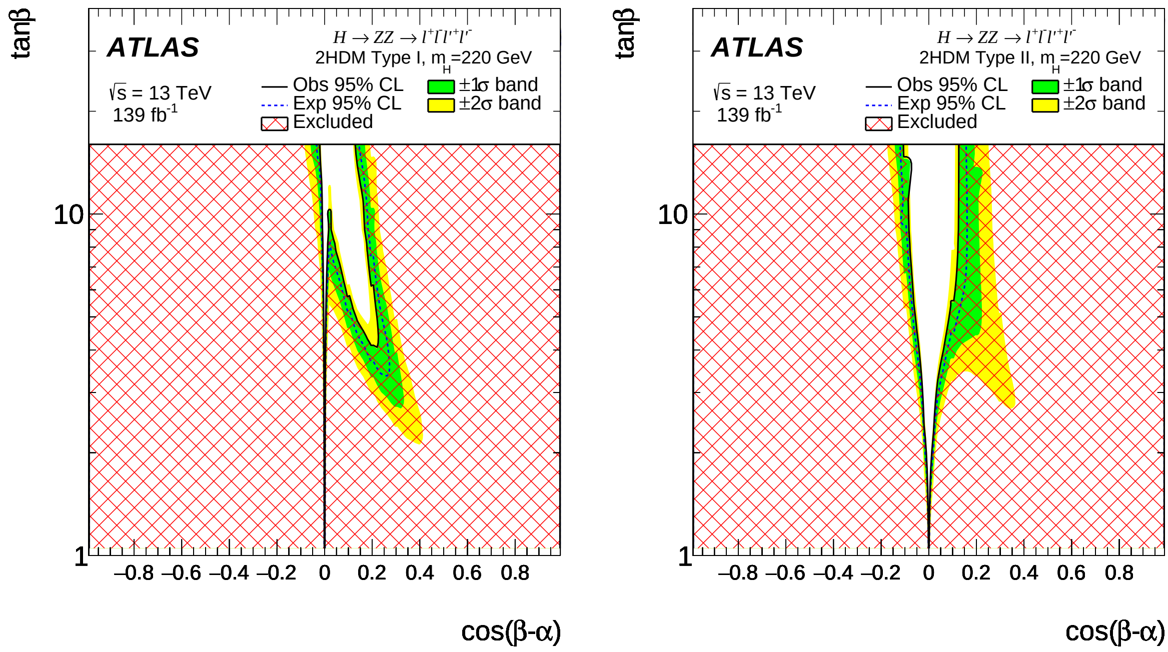

(a) (b)

Figure 8: The exclusion contour in the 2HDM (a) Type-I and (b) Type-II models for m_H = 220 GeV shown as a function of the parameters $\cos(\beta - \alpha)$ and $\tan\beta$. The green and yellow bands represent the $\pm1\sigma$ and $\pm2\sigma$ uncertainties in the expected limits. The hatched area shows the observed exclusion [9].

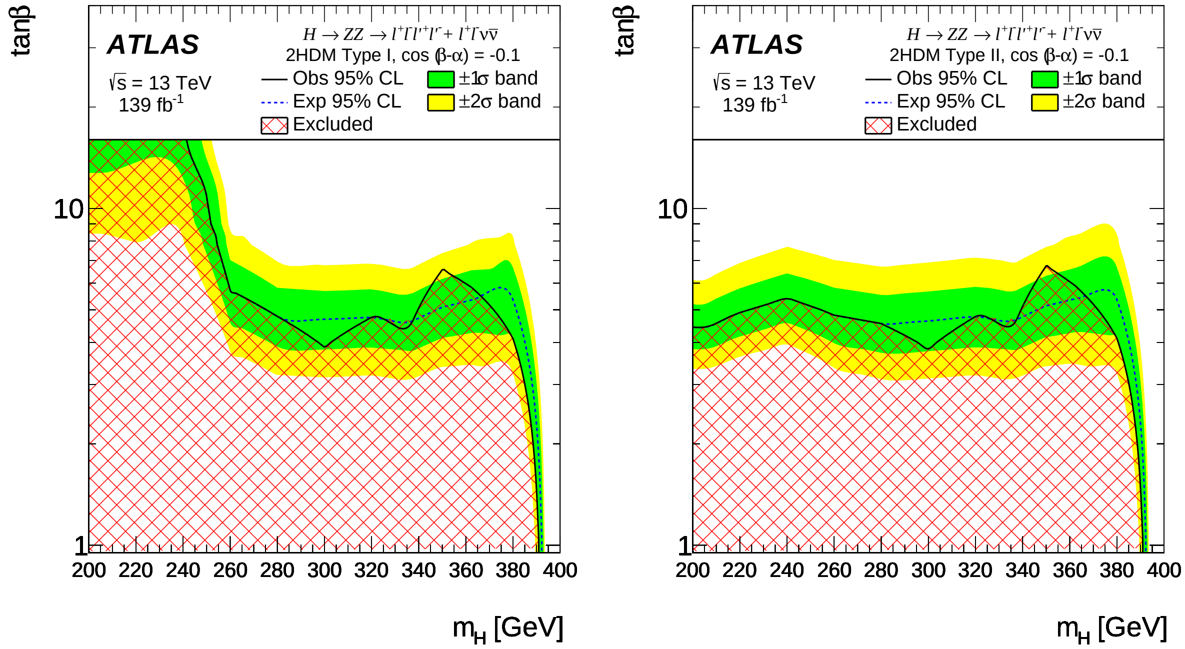

(a) (b)

Figure 9: The exclusion contour in the 2HDM (a) Type-I and (b) Type-II models for $\cos(\beta - \alpha) = -0.1$, shown as a function of the heavy scalar mass m_H and the parameter $\tan\beta$. The green and yellow bands represent the $\pm 1\sigma$ and $\pm 2\sigma$ uncertainties in the expected limits. The hatched area shows the observed exclusion [9].

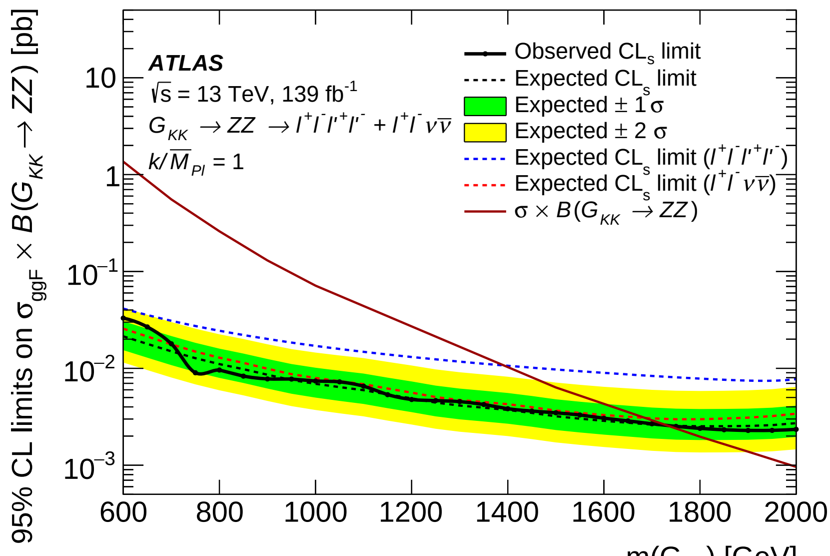

Figure 10: The upper limits at 95% CL on cross section times branching ratio $\sigma \times B(G_{\text{KK}} \to ZZ)$ for a KK graviton produced with $k/\overline{M}_{\text{Pl}} = 1$. The black line indicates the observed limit. The green and yellow bands give the $\pm 1\sigma$ and $\pm 2\sigma$ uncertainties in the expected limits. The predicted production cross section times branching ratio as a function of the G_{KK} mass $m(G_{\text{KK}})$ is shown by the red solid line [9].

10 Conclusions

A search is performed for heavy resonances decaying into a pair of Z bosons which subsequently decay into $\ell^+\ell^-\ell'^+\ell'^-$ or $\ell^+\ell^-\nu\bar{\nu}$ final states [9]. The search uses proton-proton collision data collected with the ATLAS detector from 2015 to 2018 at the LHC at a centre-of-mass energy of 13 TeV corresponding to the full Run 2 integrated luminosity of 139 fb^{-1}. No significant excess is observed with respect to the predicted SM background; therefore, the results are interpreted as upper limits on the production cross section of spin-0 resonances or a spin-2 resonance. The mass range of the hypothetical resonances considered is between 200 GeV and 2000 GeV depending on the final state and the model considered. Assuming the spin-0 resonance to be a heavy scalar, whose dominant production modes are gluon-gluon fusion (ggF) and vector-boson fusion (VBF), it is studied in both the narrow-width approximation (NWA) and the large-width assumption (LWA). In the case of the NWA, upper limits on the production rate of a heavy scalar decaying into two Z bosons (the production cross-section times the corresponding decay branching fraction) are set separately for ggF and VBF production modes. Combining the two final states, 95% CL upper limits range from 200 fb at $m_H = 240$ GeV to 2.6 fb at $m_H = 2000$ GeV for the ggF production mode and from 87 fb at $m_H = 255$ GeV to 1.9 fb at $m_H = 1800$ GeV for the VBF production mode. The results are also interpreted in the context of Type-I and Type-II two-Higgs-doublet models, with exclusion contours given in the $\tan\beta$ versus $\cos(\beta-\alpha)$ (for $m_H = 220$ GeV) and $\tan\beta$ versus m_H planes. This value of m_H is chosen so that the assumption of a narrow Higgs boson is valid over most of the parameter space and therefore the experimental sensitivity is maximal. The limits on the production rate of a large-width scalar are obtained for widths of 1%, 5%, 10% and 15% of the mass of the resonance, with the interference between the heavy scalar and the SM Higgs boson as well as between the heavy scalar and the $gg \rightarrow ZZ$ continuum taken into account. In the framework of the Randall-Sundrum model with one warped extra dimension a graviton excitation spin-2 resonance with $m(G_{KK}) < 1750$ GeV is excluded at 95% CL

References

[1] ATLAS Collaboration, *Observation of a new particle in the search for the Standard Model Higgs boson with the ATLAS detector at the LHC*, Phys. Lett. B **716** (2012) 1, arXiv: 1207.7214 [hep-ex] (cit. on p. 2).

[2] CMS Collaboration, *Observation of a new boson at a mass of 125 GeV with the CMS experiment at the LHC*, Phys. Lett. B **716** (2012) 30, arXiv: 1207.7235 [hep-ex] (cit. on p. 2).

[3] ATLAS Collaboration, *Measurements of the Higgs boson production and decay rates and coupling strengths using pp collision data at $\sqrt{s} = 7$ and 8 TeV in the ATLAS experiment*, Eur. Phys. J. C **76** (2016) 6, arXiv: 1507.04548 [hep-ex] (cit. on p. 2).

[4] CMS Collaboration, *Precise determination of the mass of the Higgs boson and tests of compatibility of its couplings with the standard model predictions using proton collisions at 7 and 8 TeV*, Eur. Phys. J. C **75** (2015) 212, arXiv: 1412.8662 [hep-ex] (cit. on p. 2).

[5] ATLAS Collaboration, *Evidence for the spin-0 nature of the Higgs boson using ATLAS data*, Phys. Lett. B **726** (2013) 120, arXiv: 1307.1432 [hep-ex] (cit. on p. 2).

[6] G. Branco et al., *Theory and phenomenology of two-Higgs-doublet models*, Phys. Rept. **516** (2012) 1, arXiv: 1106.0034 [hep-ph] (cit. on p. 3).

[7] L. Randall and R. Sundrum, *A Large mass hierarchy from a small extra dimension*, Phys. Rev. Lett. **83** (1999) 3370, arXiv: hep-ph/9905221 (cit. on p. 3).

[8] H. Davoudiasl, J. L. Hewett and T. G. Rizzo, *Bulk gauge fields in the Randall–Sundrum model*, Phys. Lett. B **473** (2000) 43, arXiv: hep-ph/9911262 (cit. on pp. 3, 5).

[9] ATLAS Collaboration, (2020), arXiv: 2009.14791 [hep-ph] (cit. on pp. 3, 4, 9–13, 15–27).

[10] ATLAS Collaboration, *Search for heavy ZZ resonances in the $\ell^+\ell^-\ell^+\ell^-$ and $\ell^+\ell^-\nu\bar{\nu}$ final states using proton–proton collisions at $\sqrt{s} = 13$ TeV with the ATLAS detector*, Eur. Phys. J. C **78** (2018) 293, arXiv: 1712.06386 [hep-ex] (cit. on pp. 3, 4, 11, 12, 14, 18, 22, 23).

[11] ATLAS Collaboration, *The ATLAS Experiment at the CERN Large Hadron Collider*, JINST **3** (2008) S08003 (cit. on p. 4).

[12] ATLAS Collaboration, *Performance of the ATLAS Trigger System in 2015*, Eur. Phys. J. C **77** (2017) 317, arXiv: 1611.09661 [hep-ex] (cit. on p. 4).

[13] ATLAS Collaboration, *ATLAS data quality operations and performance for 2015-2018 data-taking*, JINST **15** (2020) P04003, arXiv: 1911.04632 [physics.ins-det] (cit. on p. 4).

[14] ATLAS Collaboration, *The ATLAS Simulation Infrastructure*, Eur. Phys. J. C **70** (2010) 823, arXiv: 1005.4568 [physics.ins-det] (cit. on p. 5).

[15] S. Agostinelli et al., *GEANT4: A simulation toolkit*, Nucl. Instrum. Meth. A **506** (2003) 250 (cit. on p. 5).

[16] T. Sjöstrand, S. Mrenna and P. Z. Skands, *A brief introduction to PYTHIA 8.1*, Comput. Phys. Commun. **178** (2008) 852, arXiv: 0710.3820 [hep-ph] (cit. on p. 5).

[17] ATLAS Collaboration, *Summary of ATLAS Pythia 8 tunes*, ATL-PHYS-PUB-2012-003, 2012, URL: https://cds.cern.ch/record/1474107 (cit. on p. 5).

[18] A. D. Martin, W. J. Stirling, R. S. Thorne and G. Watt, *Parton distributions for the LHC*, Eur. Phys. J. C **63** (2009) 189, arXiv: 0901.0002 [hep-ph] (cit. on p. 5).

[19] P. Nason and G. Zanderighi, *W^+W^-, WZ and ZZ production in the POWHEG-BOX-V2*, Eur. Phys. J. C **74** (2014) 2702, arXiv: 1311.1365 [hep-ph] (cit. on p. 5).

[20] T. Sjöstrand et al., *An introduction to PYTHIA 8.2*, Comput. Phys. Commun. **191** (2015) 159, arXiv: 1410.3012 [hep-ph] (cit. on p. 5).

[21] ATLAS Collaboration, *Measurement of the Z/γ^* boson transverse momentum distribution in pp collisions at $\sqrt{s} = 7$ TeV with the ATLAS detector*, JHEP **09** (2014) 145, arXiv: 1406.3660 [hep-ex] (cit. on p. 5).

[22] D. J. Lange, *The EvtGen particle decay simulation package*, Nucl. Instrum. Meth. A **462** (2001) 152 (cit. on p. 5).

[23] H.-L. Lai et al., *New parton distributions for collider physics*, Phys. Rev. D **82** (2010) 074024, arXiv: 1007.2241 [hep-ph] (cit. on p. 5).

[24] J. Alwall et al., *The automated computation of tree-level and next-to-leading order differential cross sections, and their matching to parton shower simulations*, JHEP **07** (2014) 079, arXiv: 1405.0301 [hep-ph] (cit. on p. 5).

[25] ATLAS Collaboration, *ATLAS Pythia 8 tunes to 7 TeV data*, ATL-PHYS-PUB-2014-021, 2014, URL: https://cds.cern.ch/record/1966419 (cit. on p. 5).

[26] K. Agashe, H. Davoudiasl, G. Perez and A. Soni, *Warped gravitons at the CERN LHC and beyond*, Phys. Rev. D **76** (3 2007) 036006 (cit. on p. 5).

[27] R. D. Ball et al., *Parton distributions for the LHC Run II*, JHEP **04** (2015) 040, arXiv: 1410.8849 [hep-ph] (cit. on p. 6).

[28] E. Bothmann et al., *Event generation with Sherpa 2.2*, SciPost Phys. **7** (2019) 034, arXiv: 1905.09127 [hep-ph] (cit. on p. 6).

[29] T. Gleisberg and S. Höche, *Comix, a new matrix element generator*, JHEP **12** (2008) 039, arXiv: 0808.3674 [hep-ph] (cit. on p. 6).

[30] F. Buccioni et al., *OpenLoops 2*, Eur. Phys. J. C **79** (2019) 866, arXiv: 1907.13071 [hep-ph] (cit. on p. 6).

[31] F. Cascioli, P. Maieröfer and S. Pozzorini, *Scattering Amplitudes with Open Loops*, Phys. Rev. Lett. **108** (2012) 111601, arXiv: 1111.5206 [hep-ph] (cit. on p. 6).

[32] A. Denner, S. Dittmaier and L. Hofer, *Collier: A fortran-based complex one-loop library in extended regularizations*, Comput. Phys. Commun. **212** (2017) 220, arXiv: 1604.06792 [hep-ph] (cit. on p. 6).

[33] S. Schumann and F. Krauss, *A Parton shower algorithm based on Catani-Seymour dipole factorisation*, JHEP **03** (2008) 038, arXiv: 0709.1027 [hep-ph] (cit. on p. 6).

[34] S. Höche, F. Krauss, M. Schönherr and F. Siegert, *QCD matrix elements + parton showers. The NLO case*, JHEP **04** (2013) 027, arXiv: 1207.5030 [hep-ph] (cit. on p. 6).

[35] B. Biedermann, A. Denner, S. Dittmaier, L. Hofer and B. Jäger, *Electroweak Corrections to $pp \to \mu^+\mu^-e^+e^- + X$ at the LHC: A Higgs Boson Background Study*, Phys. Rev. Lett. **116** (2016) 161803, arXiv: 1601.07787 [hep-ph] (cit. on pp. 6, 18).

[36] B. Biedermann, A. Denner, S. Dittmaier, L. Hofer and B. Jäger, *Next-to-leading-order electroweak corrections to the production of four charged leptons at the LHC*, JHEP **01** (2017) 033, arXiv: 1611.05338 [hep-ph] (cit. on pp. 6, 18).

[37] S. Kallweit, J. M. Lindert, P. Maierhöfer, S. Pozzorini and M. Schönherr, *NLO electroweak automation and precise predictions for W+multijet production at the LHC*, JHEP **04** (2015) 012, arXiv: 1412.5157 [hep-ph] (cit. on p. 6).

[38] S. Kallweit, J. Lindert, S. Pozzorini and M. Schönherr, *NLO QCD+EW predictions for $2\ell2\nu$ diboson signatures at the LHC*, JHEP **11** (2017) 120, arXiv: 1705.00598 [hep-ph] (cit. on pp. 6, 18).

[39] M. Schönherr, *An automated subtraction of NLO EW infrared divergences*, Eur. Phys. J. C **78** (2018) 119, arXiv: 1712.07975 [hep-ph] (cit. on p. 6).

[40] M. Grazzini, S. Kallweit, J. M. Lindert, S. Pozzorini and M. Wiesemann, *NNLO QCD + NLO EW with Matrix+OpenLoops: precise predictions for vector-boson pair production*, JHEP **02** (2020) 087, arXiv: 1912.00068 [hep-ph] (cit. on p. 6).

[41] F. Caola, K. Melnikov, R. Röntsch and L. Tancredi, *QCD corrections to ZZ production in gluon fusion at the LHC*, Phys. Rev. D **92** (2015) 094028, arXiv: 1509.06734 [hep-ph] (cit. on p. 6).

[42] J. M. Campbell, R. K. Ellis, M. Czakon and S. Kirchner, *Two loop correction to interference in $gg \to ZZ$*, JHEP **08** (2016) 011, arXiv: 1605.01380 [hep-ph] (cit. on p. 6).

[43] S. Alioli, F. Caola, G. Luisoni and R. Röntsch, *ZZ production in gluon fusion at NLO matched to parton-shower*, Phys. Rev. D **95** (2017) 034042, arXiv: 1609.09719 [hep-ph] (cit. on p. 6).

[44] K. Melnikov and M. Dowling, *Production of two Z-bosons in gluon fusion in the heavy top quark approximation*, Phys. Lett. B **744** (2015) 43, arXiv: 1503.01274 [hep-ph] (cit. on p. 6).

[45] C. S. Li, H. T. Li, D. Y. Shao and J. Wang, *Soft gluon resummation in the signal-background interference process of gg(→ h^*)→ ZZ*, JHEP **08** (2015) 065, arXiv: 1504.02388 [hep-ph] (cit. on p. 6).

[46] R. Gavin, Y. Li, F. Petriello and S. Quackenbush, *FEWZ 2.0: A code for hadronic Z production at next-to-next-to-leading order*, Comput. Phys. Commun. **182** (2011) 2388, arXiv: 1011.3540 [hep-ph] (cit. on p. 6).

[47] S. Frixione, V. Hirschi, D. Pagani, H.-S. Shao and M. Zaro, *Electroweak and QCD corrections to top-pair hadroproduction in association with heavy bosons*, JHEP **06** (2015) 184, arXiv: 1504.03446 [hep-ph] (cit. on p. 6).

[48] J. M. Campbell, R. K. Ellis and C. Williams, *Vector boson pair production at the LHC*, JHEP **07** (2011) 18, arXiv: 1105.0020 [hep-ph] (cit. on p. 7).

[49] N. Kauer and G. Passarino, *Inadequacy of zero-width approximation for a light Higgs boson signal*, JHEP **08** (2012) 116, arXiv: 1206.4803 [hep-ph] (cit. on p. 7).

[50] N. Kauer, *Interference effects for $H \rightarrow WW/ZZ \rightarrow \ell\bar{\nu}_\ell\bar{\ell}\nu_\ell$ searches in gluon fusion at the LHC*, JHEP **12** (2013) 082, arXiv: 1310.7011 [hep-ph] (cit. on p. 7).

[51] ATLAS Collaboration, *Electron and photon performance measurements with the ATLAS detector using the 2015–2017 LHC proton–proton collision data*, JINST **14** (2019) P12006, arXiv: 1908.00005 [hep-ex] (cit. on p. 7).

[52] ATLAS Collaboration, *Improved electron reconstruction in ATLAS using the Gaussian Sum Filter-based model for bremsstrahlung*, ATLAS-CONF-2012-047, 2012, URL: https://cds.cern.ch/record/1449796 (cit. on p. 7).

[53] ATLAS Collaboration, *Electron reconstruction and identification in the ATLAS experiment using the 2015 and 2016 LHC proton–proton collision data at $\sqrt{s}$ = 13 TeV*, Eur. Phys. J. C **79** (2019) 639, arXiv: 1902.04655 [hep-ex] (cit. on pp. 7, 17).

[54] ATLAS Collaboration, *Muon reconstruction performance of the ATLAS detector in proton–proton collision data at $\sqrt{s}$ = 13 TeV*, Eur. Phys. J. C **76** (2016) 292, arXiv: 1603.05598 [hep-ex] (cit. on pp. 7, 17).

[55] ATLAS Collaboration, *Jet reconstruction and performance using particle flow with the ATLAS Detector*, Eur. Phys. J. C **77** (2017) 466, arXiv: 1703.10485 [hep-ex] (cit. on p. 7).

[56] ATLAS Collaboration, *Topological cell clustering in the ATLAS calorimeters and its performance in LHC Run 1*, Eur. Phys. J. C **77** (2017) 490, arXiv: 1603.02934 [hep-ex] (cit. on p. 7).

[57] M. Cacciari, G. P. Salam and G. Soyez, *The anti-k_t jet clustering algorithm*, JHEP **04** (2008) 063, arXiv: 0802.1189 [hep-ph] (cit. on p. 7).

[58] ATLAS Collaboration, *Jet energy scale measurements and their systematic uncertainties in proton-proton collisions at $\sqrt{s}$ = 13 TeV with the ATLAS detector*, Phys. Rev. D **96** (2017) 072002, arXiv: 1703.09665 [hep-ex] (cit. on p. 7).

[59] ATLAS Collaboration, *Tagging and suppression of pileup jets with the ATLAS detector*, tech. rep. ATLAS-CONF-2014-018, CERN, 2014, URL: https://cds.cern.ch/record/1700870 (cit. on p. 7).

[60] ATLAS Collaboration, *Performance of pile-up mitigation techniques for jets in pp collisions at $\sqrt{s}$ = 8 TeV using the ATLAS detector*, Eur. Phys. J. C **76** (2016) 581, arXiv: 1510.03823 [hep-ex] (cit. on p. 7).

[61] ATLAS Collaboration, *ATLAS b-jet identification performance and efficiency measurement with $t\bar{t}$ events in pp collisions at $\sqrt{s} = 13$ TeV*, Eur. Phys. J. C **79** (2019) 970, arXiv: 1907.05120 [hep-ex] (cit. on p. 7).

[62] ATLAS Collaboration, *Performance of missing transverse momentum reconstruction with the ATLAS detector using proton-proton collisions at $\sqrt{s}$ = 13 TeV*, Eur. Phys. J. C **78** (2018) 903, arXiv: 1802.08168 [hep-ex] (cit. on p. 7).

[63] ATLAS Collaboration, *2015 start-up trigger menu and initial performance assessment of the ATLAS trigger using Run-2 data*, ATL-DAQ-PUB-2016-001, 2016, URL: https://cds.cern.ch/record/2136007 (cit. on p. 8).

[64] ATLAS Collaboration, *Trigger Menu in 2016*, ATL-DAQ-PUB-2017-001, 2017, URL: https://cds.cern.ch/record/2242069 (cit. on p. 8).

[65] ATLAS Collaboration, *Search for an additional, heavy Higgs boson in the $H \to ZZ$ decay channel at $\sqrt{s} = 8$ TeV in pp collision data with the ATLAS detector*, Eur. Phys. J. C **76** (2016) 45, arXiv: 1507.05930 [hep-ex] (cit. on p. 8).

[66] ATLAS Collaboration, *Measurement of the Higgs boson mass from the $H \to \gamma\gamma$ and $H \to ZZ^* \to 4\ell$ channels in pp collisions at center-of-mass energies of 7 and 8 TeV with the ATLAS detector*, Phys. Rev. D **90** (2014) 052004, arXiv: 1406.3827 [hep-ex] (cit. on p. 9).

[67] ATLAS Collaboration, *Higgs boson production cross-section measurements and their EFT interpretation in the 4ℓ decay channel at $\sqrt{s}$ = 13 TeV with the ATLAS detector*, (2020), arXiv: 2004.03447 [hep-ex] (cit. on p. 9).

[68] M. Abadi et al., *TensorFlow: Large-Scale Machine Learning on Heterogeneous Systems*, 2015, URL: https://www.tensorflow.org/ (cit. on p. 9).

[69] ATLAS Collaboration, *Measurement of inclusive and differential cross sections in the $H \to ZZ^* \to 4\ell$ decay channel in pp collisions at $\sqrt{s} = 13$ TeV with the ATLAS detector*, JHEP **10** (2017) 132, arXiv: 1708.02810 [hep-ex] (cit. on p. 11).

[70] ATLAS Collaboration, *Measurement of the Higgs boson coupling properties in the $H \to ZZ^* \to 4\ell$ decay channel at $\sqrt{s} = 13$ TeV with the ATLAS detector*, JHEP **03** (2018) 095, arXiv: 1712.02304 [hep-ex] (cit. on p. 11).

[71] M. Oreglia, *A Study of the Reactions $\psi' \to \gamma\gamma\psi$*, 1980, URL: https://www.slac.stanford.edu/cgi-wrap/getdoc/slac-r-236.pdf (cit. on p. 11).

[72] J. Gaiser, *Charmonium Spectroscopy From Radiative Decays of the J/ψ and ψ'*, 1982, URL: https://www.slac.stanford.edu/cgi-wrap/getdoc/slac-r-255.pdf (cit. on p. 11).

[73] S. Goria, G. Passarino and D. Rosco, *The Higgs-boson lineshape*, Nucl. Phys. B **864** (2012) 530, arXiv: 1112.5517 [hep-ph] (cit. on p. 12).

[74] N. Kauer and C. O'Brien, *Heavy Higgs signal-background interference in $gg \to VV$ in the Standard Model plus real singlet*, Eur. Phys. J. C **75** (2015) 374, arXiv: 1502.04113 [hep-ph] (cit. on p. 13).

[75] ATLAS Collaboration, *Object-based missing transverse momentum significance in the ATLAS Detector*, ATLAS-CONF-2018-038, 2018, URL: https://cds.cern.ch/record/2630948 (cit. on p. 15).

[76] ATLAS Collaboration, *Measurement of $W^{\pm}Z$ production cross sections and gauge boson polarisation in pp collisions at $\sqrt{s} = 13$ TeV with the ATLAS detector*, Eur. Phys. J. C **79** (2019) 535, arXiv: 1902.05759 [hep-ex] (cit. on p. 16).

[77] ATLAS Collaboration, *Observation of electroweak $W^{\pm}Z$ boson pair production in association with two jets in pp collisions at $\sqrt{s} = 13$ TeV with the ATLAS detector*, Phys. Lett. B **793** (2019) 469, arXiv: 1812.09740 [hep-ex] (cit. on p. 16).

[78] M. Baak, S. Gadatsch, R. Harrington and W. Verkerke, *Interpolation between multi-dimensional histograms using a new non-linear moment morphing method*, Nucl. Instrum. Meth. A **771** (2015) 39, arXiv: 1410.7388 [physics.data-an] (cit. on p. 16).

[79] ATLAS Collaboration, *Luminosity determination in pp collisions at $\sqrt{s} = 13$ TeV using the ATLAS detector at the LHC*, ATLAS-CONF-2019-021, 2019, URL: https://cds.cern.ch/record/2677054 (cit. on p. 17).

[80] G. Avoni et al., *The new LUCID-2 detector for luminosity measurement and monitoring in ATLAS*, JINST **13** (2018) P07017 (cit. on p. 17).

[81] ATLAS Collaboration, *Jet energy scale measurements and their systematic uncertainties in proton–proton collisions at $\sqrt{s} = 13$ TeV with the ATLAS detector*, Phys. Rev. D **96** (2017) 072002, arXiv: 1703.09665 [hep-ex] (cit. on p. 17).

[82] ATLAS Collaboration, *Performance of missing transverse momentum reconstruction with the ATLAS detector using proton–proton collisions at $\sqrt{s} = 13$ TeV*, Eur. Phys. J. C **78** (2018) 903, arXiv: 1802.08168 [hep-ex] (cit. on p. 17).

[83] J. Butterworth et al., *PDF4LHC recommendations for LHC Run II*, J. Phys. G **43** (2016) 023001, arXiv: 1510.03865 [hep-ph] (cit. on p. 17).

[84] ATLAS and CMS Collaboration, *Procedure for the LHC Higgs boson search combination in summer 2011*, ATL-PHYS-PUB-2011-011, CMS-NOTE-2011-005, 2011, URL: https://cds.cern.ch/record/1375842 (cit. on p. 18).

[85] ATLAS Collaboration, *Combined search for the Standard Model Higgs boson in pp collisions at $\sqrt{s} = 7$ TeV with the ATLAS detector*, Phys. Rev. D **86** (2012) 032003, arXiv: 1207.0319 [hep-ex] (cit. on p. 18).

[86] A. L. Read, *Presentation of search results: the CL_S technique*, J. Phys. G **28** (2002) 2693 (cit. on p. 20).

[87] ATLAS Collaboration, *Combined measurements of Higgs boson production and decay using up to 80 fb^{-1} of proton–proton collision data at $\sqrt{s} = 13$ TeV collected with the ATLAS experiment*, Phys. Rev. D **101** (2020) 012002, arXiv: 1909.02845 [hep-ex] (cit. on p. 23).